RESEARCH ARTICLE

Key Points:
- Two-dimensional L-MLT plots of average electron, H^{+}, He^{+}, and O[+] fluxes and ion flux ratios show significant structure and dependence on energy and Kp
- A new afternoon bulge plasma population enriched in 10 keV O[+] and He^{+} is observed for Kp < 5 at ~1100–2000 MLT and L shell range 2–4
- A new tool built on UBK modeling classifies plasma sheet particle access to the inner magnetosphere

Supporting Information:
- Supporting Information S1

Correspondence to:
P. A. Fernandes,
pfernandes@lanl.gov

The plasma environment inside geostationary orbit: A Van Allen Probes HOPE survey

Philip A. Fernandes[1,2] (iD), **Brian A. Larsen**[1,2] (iD), **Michelle F. Thomsen**[3] (iD), **Ruth M. Skoug**[1,2] (iD), **Geoffrey D. Reeves**[1,2] (iD), **Michael H. Denton**[2,4] (iD), **Reinhard H. W. Friedel**[2,5] (iD), **Herbert O. Funsten**[1] (iD), **Jerry Goldstein**[6] (iD), **Michael G. Henderson**[1,2] (iD), **Jörg-Micha Jahn**[6] (iD), **Elizabeth A. MacDonald**[7] (iD), and **David K. Olson**[1] (iD)

[1]ISR-1, Los Alamos National Laboratory, Los Alamos, New Mexico, USA, [2]New Mexico Consortium, Los Alamos, New Mexico, USA, [3]Planetary Science Institute, Tucson, Arizona, USA, [4]Space Science Institute, Boulder, Colorado, USA, [5]CSES, Los Alamos National Laboratory, Los Alamos, New Mexico, USA, [6]Department of Space Science, Southwest Research Institute, San Antonio, Texas, USA, [7]NASA Goddard Space Flight Center, Greenbelt, Maryland, USA

Abstract The two full precessions in local time completed by the Van Allen Probes enable global specification of the near-equatorial inner magnetosphere plasma environment. Observations by the Helium-Oxygen-Proton-Electron (HOPE) mass spectrometers provide detailed insight into the global spatial distribution of electrons, H^{+}, He^{+}, and O[+]. Near-equatorial omnidirectional fluxes and abundance ratios at energies 0.1–30 keV are presented for $2 \leq L \leq 6$ as a function of L shell, magnetic local time (MLT), and geomagnetic activity. We present a new tool built on the UBK modeling technique for classifying plasma sheet particle access to the inner magnetosphere. This new tool generates access maps for particles of constant energy for more direct comparison with in situ measurements, rather than the traditional constant μ presentation typically associated with UBK. We present for the first time inner magnetosphere abundances of O[+] flux relative to H^{+} flux as a function of Kp, L, MLT, and energy. At $L = 6$, the O[+]/H^{+} ratio increases with increasing Kp, consistent with previous results. However, at $L < 5$ the O[+]/H^{+} ratio generally decreases with increasing Kp. We identify a new "afternoon bulge" plasma population enriched in 10 keV O[+] and superenriched in 10 keV He[+] that is present during quiet/moderate geomagnetic activity ($Kp < 5$) at ~1100–2000 MLT and L shell 2–4. Drift path modeling results are consistent with the narrow energy and approximate MLT location of this enhancement, but the underlying physics describing its formation, structure, and depletion during higher geomagnetic activity are currently not understood.

Plain Language Summary We present a detailed study of the composition of the equatorial plane of the inner magnetosphere using 40 months of electron and ion data from the HOPE mass spectrometers on the Van Allen Probes spacecraft. Specifically, we present 2-D distributions of fluxes of electrons, H^{+}, O[+], and He^{+}, as well as flux ratios of O[+]/H^{+}, He^{+}/H^{+}, and He^{+}/O[+]. This study builds on historical characterization of the equatorial plasma environment. These previous studies have various shortcomings, including limited 2-D coverage due to the nature of their spacecraft orbits and severe contamination of measurements due to the significant background induced by penetrating radiation inherent in the radiation belts. This study advances the field by presenting the most comprehensive measurements of electrons and ion species to date using instrumentation specifically designed to mitigate background effects. In this study, we establish a new tool built upon well-established modeling and use this tool to analyze the data by classifying regions to which certain particle populations may or may not have access. Our analysis identifies a new plasma population enriched in both 10 keV O[+] and He^{+} that we call the "afternoon bulge" that is persistently present near the Earth during geomagnetically quiet conditions.

1. Introduction

The Earth's inner magnetosphere (L < 8) contains numerous distinct charged particle populations that vary by composition, energy, location, and time according to several different physical processes but nevertheless behave as a strongly coupled system. The energy extremes of this region span sub-eV cold ions in the plasmasphere [*Sojka et al.*, 1983] to relativistic electrons and protons in the radiation belts with energies up to hundreds of MeV [*McIlwain*, 1963; *Pfitzer and Winckler*, 1968].

The primary source of ~0.1–50 keV ions and electrons in the inner magnetosphere is convection of plasma sheet particles. The plasma sheet lies in the near-equatorial plane and separates the northern and southern magnetic lobes of the magnetotail. Charged particle trajectories in the Earth's inner magnetosphere are governed by the electric and magnetic fields in this region. The $E \times B$ drift associated with the electric fields acts in the same direction for both ions and electrons and is independent of particle energy or mass. The total convection electric field in its simplest approximation is the superposition of the dawn-dusk and corotation electric fields. The dawn-dusk electric field results in Earthward convection of plasma from the tail. The corotation electric field vector points inward (toward the Earth) and drives the plasma eastward as it convects into the inner magnetosphere from the magnetotail. In contrast to these electric field drifts, particle drifts due to the gradient and curvature of Earth's magnetic field are independent of mass and proportional to the particle energy per charge, driving electrons eastward and ions westward. The net drift of a charged particle is a combination of these processes whose relative importance is energy and charge dependent. Lower energy particles (approximately tens to hundreds of eV) are most heavily influenced by electric drifts, whereas higher-energy particles ($\geq$10 keV) are typically dominated by magnetic field drifts. Particles of intermediate energies may have complicated drift paths that are more equally influenced by both magnetic field and electric field drifts. A comprehensive discussion of particle drifts can be found in *Roederer and Zhang* [2014].

Particle drift paths can be determined using the UBK framework [*Whipple*, 1978]; this powerful method describes access of plasma sheet particles to the inner magnetosphere without requiring computer-intensive particle tracing [*Sheldon and Spence*, 1997; *Whipple et al.*, 1998; *Korth et al.*, 1999; *Friedel et al.*, 2001]. The UBK framework assumes particles conserve total (kinetic and potential) energy and the first adiabatic invariant along their trajectories. That total energy W_{tot} can be written as follows:

$$W_{tot} = qU + \mu B_m,$$

where B_m is the magnetic field strength at the mirror point, q is the particle charge, and U is the total scalar electric potential resulting from the dawn-dusk and corotation electric fields. The magnetic moment is defined as $\mu = E_\perp/B$ where B is the magnetic field strength at the location of the particle and the perpendicular energy $E_\perp$ is derived from the velocity component perpendicular to the magnetic field. In the UBK coordinate system, particles follow straight line trajectories with slope $-\mu/q$. Near the Earth, ions and electrons typically follow closed trajectories which are inaccessible by convection from the plasma sheet. They originate from the ionosphere and are thus typically cold. At larger distances from Earth, hotter particles are transported in from the plasma sheet. The boundary separating these open and closed regions is the Alfvén layer, often referred to as the open/closed drift boundary or separatrix.

The location of the Alfvén layer depends on particle charge, energy, and geomagnetic activity level, the latter being a proxy for the strength of the convection electric field [e.g., *Thomsen*, 2004]. A detailed description of Alfvén layers for both ions and electrons is presented by *Korth et al.* [1999]. Here we summarize these dependencies for ions (Figure 1) in a dipole magnetic field using the UBK formalism with a Volland-Stern electric field model [*Volland*, 1973; *Stern*, 1975] parameterized by the geomagnetic activity index *Kp* using the Maynard method [*Maynard and Chen*, 1975]. The Volland-Stern electric field model is time independent and therefore does not account for the well-known variable response of the inner magnetosphere electric field to geomagnetic activity [e.g., *Rowland and Wygant*, 1998]. Modeling and observations have shown the development of strong storm time electric fields which penetrate down to ionospheric altitudes [*Fok et al.*, 2001; *Ridley and Liemohn*, 2002; *Nishimura et al.*, 2007; *Mannucci et al.*, 2009]. Our usage of the Volland-Stern electric field model means that our implementation of UBK formalism is limited to time-averaged statistical analysis.

Fundamental to the UBK method is the conservation of the first adiabatic invariant: $\mu = E_\perp/B$ is constant. The Alfvén layers shown in Figures 1a–1h are derived for particles of constant μ, calculated for perpendicular energy of 0.3, 1, 3, and 10 keV at L = 6. The left column shows the boundaries for *Kp* = 1.0 and the right column for *Kp* = 5.3. The Alfvén layer for a given μ is closest to Earth for low-energy particles during strong convection. Correspondingly, this Alfvén layer is found at larger distances for higher energy particles or during less geomagnetically active times. For lower energy electrons and ions (approximately tens of eV up to ~1 keV of eV up to ~1 keV), electric field drifts dominate and the Alfvén layer is teardrop shaped with the stagnation point in the dusk sector (Figures 1a–1c). For higher energy ions at sufficient *Kp*, magnetic
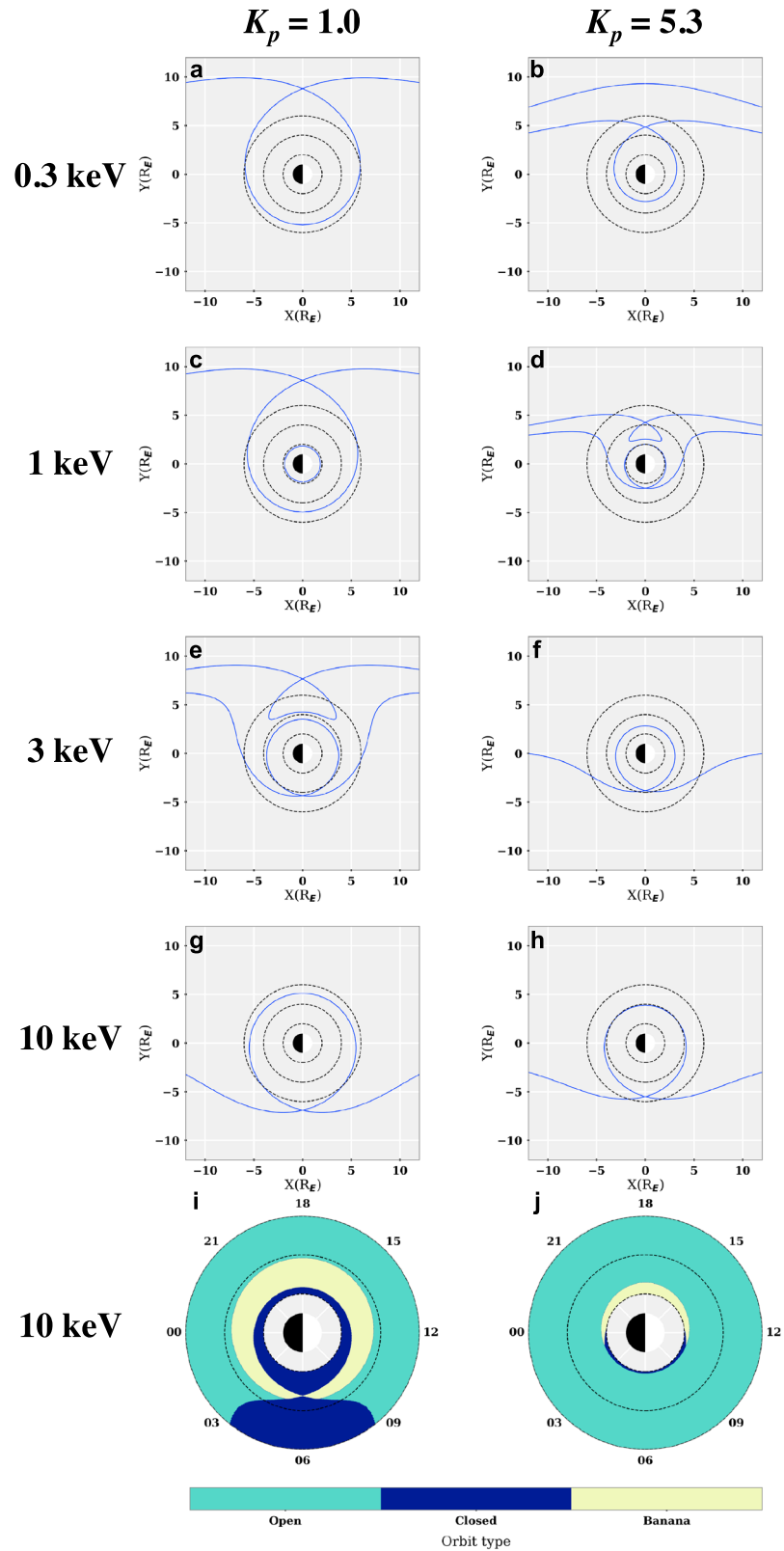
Figure 1. (a–h) Alfvén layers are derived for particles of constant μ, calculated for perpendicular energies of 0.3, 1, 3, and 10 keV at L = 6. The left column shows the boundaries for Kp = 1.0 and the right column for Kp = 5.3. (i and j) Ion access maps for particles with 10 keV perpendicular energy calculated using the UBK formalism. Mapping of the Alfvén layer plots to the ion access maps is discussed in the text.

field drifts dominate and the Alfvén layer is teardrop shaped with the stagnation point in the dawn sector (Figures 1f–1h). At intermediate energies and geomagnetic activity level, the magnetic and electric field effects are comparable leading to complicated charged particle dynamics. This influences the shape of the Alfvén layer as "banana orbits" [*Strangeway and Johnson*, 1984] can form in the dusk sector (Figures 1d and 1e). Additionally, charged particles at these intermediate energies are able to penetrate deeper into the magnetosphere leading to observation of "nose-like" structures in energy-time spectrograms [e.g., *Smith and Hoffman*, 1974; *Ejiri*, 1978; *Ejiri et al.*, 1980].

For this study, we analyze in situ measurements of charged particle distributions in the context of their trajectories as predicted by the UBK formalism. All analysis in this study assumes that particles and their trajectories lie in the equatorial plane ($K = 0$ in the UBK framework). We expand on the UBK formalism to develop a new analysis tool: constant perpendicular energy access maps, as shown in Figures 1i and 1j. These constant energy access maps provide no direct information about particle trajectories, a significant deviation from the traditional usage of UBK to determine the location of the Alfvén layer (as shown in Figures 1a–1h). Rather, these access maps are a tool for organizing the orbit type of particles of a defined energy located at a particular L-MLT coordinate. These constant energy access maps better correspond to particle measurements at a single energy, as is typical of in situ observations.

For the access maps shown in Figures 1i and 1j, ions with 10 keV perpendicular energy are examined at each L shell and magnetic local time (L and MLT) coordinate in the equatorial plane. The UBK methodology is used to determine if a particle with 10 keV perpendicular energy at each location is on an open drift path, a closed orbit, or a banana orbit. Ions with 10 keV perpendicular energy have different values of μ at different distances. An ion at small radial distance has a significantly larger μ than a particle at a larger distance, because while these particles have the same perpendicular energy, the magnetic field strength B decreases with radial distance.

The features in these 10 keV ion access maps (Figures 1i and 1j) can be understood in the context of the Alfvén layers for constant μ. Ions at L = 6 in the access maps (Figures 1i and 1j) correspond to the constant μ trajectories shown in Figures 1g and 1h, in which μ is defined for ions with 10 keV perpendicular energy at L = 6. The Alfvén boundary for 10 keV ions at low Kp (Figure 1g) exhibits a stagnation point in the dawn sector extending beyond L = 6. Inside this stagnation point, particles are on closed drift paths; at L = 6, the closed region extends from approximately 0330–0830 MLT. The corresponding access map (Figure 1i) shows the same region of closed drift paths at L = 6 and 0330–0830 MLT. Particles near L = 4 on this access map (Figure 1i) again have 10 keV perpendicular energy and therefore a smaller μ compared to 10 keV particles at L = 6. To conserve W_{tot} and μ, these particles must have been perpendicularly energized when transported to smaller L. Specifically, 10 keV particles at L = 4 would have had 3 keV perpendicular energy at L = 6 and thus follow the trajectories shown in Figure 1e. Examining trajectories for ions at L = 4 in Figure 1e, the ions are on open trajectories except for a small region of closed trajectories from ~0400 to 0800 MLT. The access map (Figure 1i) shows the same open/closed boundaries at L = 4. Finally, at L = 2 on the access map (Figure 1i) all particles lie on closed trajectories. Particles with 10 keV perpendicular energy at L = 2 have a μ which corresponds to ~0.3 keV perpendicular energy at L = 6, and thus, these particles are associated with the 0.3 keV trajectory plot shown in Figure 1a. In this figure, all particles at L = 2 lie on closed trajectories, consistent with the access map (Figure 1i). A similar comparison describes the features in the high Kp access map (Figure 1j) based on the Alfvén layers in Figures 1b, 1d, 1f, and 1h.

The composition of the inner magnetosphere is of great importance to wave and energetic particle processes in this region [*Friedel et al.*, 2002; *Singh et al.*, 2011]. In turn, the numerous plasma waves generated within the inner magnetosphere play an important role in acceleration, energetic particle dynamics, and, more broadly, magnetosphere-ionosphere coupling [*Gendrin*, 1975]. Local plasma composition influences both the frequency at which plasma waves are generated and their growth or attenuation rate. Interactions of particles with various plasma waves are the driver behind many of the loss mechanisms in the radiation belts [e.g., *Thorne*, 2010, and references therein]. These low energy plasma populations serve as the seed population for higher energy populations; in turn, the plasma and energetic particle populations influence wave generation which then drive radiation belt dynamics. For example, low energy (eV to tens of keV) abundances and anisotropy of He^+ and O^+ play an important role in the generation and propagation characteristics of electromagnetic ion cyclotron waves [*Young et al.*, 1981; *Gomberoff and Neira*, 1983]. The relative total densities of

ions comprising the plasma affect plasma wave stop bands, the frequency range at which a wave cannot propagate [*Kozyra et al.*, 1984]. O^+ in the plasma sheet with energy ~5–60 keV has been shown to strongly contribute to the ring current [*Kistler et al.*, 2016]. Source and loss mechanisms can be species dependent, and thus, by understanding the variation in inner magnetosphere plasma composition, we derive information about plasma sources, losses, and transport.

Previous studies of composition-resolved plasma conditions in the inner magnetosphere have been limited in L-MLT coverage due to the limited variety of spacecraft orbits. Early comprehensive investigations with ISEE and GEOS were conducted at magnetospheric distances of L > 3 [*Balsiger*, 1981; *Williams*, 1981]. Studies showed dayside O^+ with dispersion signatures characteristic of transport from the nightside [*Lennartsson et al.*, 1979], and some studies characterized the heavier, lower abundance ion species [*Leske and Wiedenbeck*, 1993]. During the CRRES mission in the 1990s the MICS instrument [*Wilken et al.*, 1992] provided measurements across a variety of geomagnetic activity conditions [*Fu et al.*, 2001; *Liu et al.*, 2005; *Forster et al.*, 2013], though these measurements are predominantly at higher energies (1–430 keV/q) than are the focus of this study. These studies found that the main injection region of plasma from the plasma sheet is located just prior to midnight and that substorms may play an important role in the transport of plasma to subgeosynchronous altitudes [*Perry et al.*, 1996]. Studies using Active Magnetospheric Particle Tracer Explorer/CCE and ISEE-2 composition measurements showed that the ionosphere more strongly contributes to magnetospheric plasma populations nearer Earth, while the solar wind is the stronger contributor to magnetospheric plasma farther from the Earth [*Gloeckler and Hamilton*, 1987; *Fuselier et al.*, 1999]. Recent studies of ion nose structures in the inner magnetosphere showed that heavy ion noses penetrate to lower L shell than H^+ noses in the afternoon sector during quiet geomagnetic conditions [*Ferradas et al.*, 2015, 2016b]. These ion nose studies used a steady state ion drift path model to characterize inner magnetospheric access of ion nose structures. This model calculated bounce-average drift trajectories of 90° pitch angle particles using the Volland-Stern electric field model and a dipole magnetic field.

Numerous studies have provided insight into plasma composition changes as a function of geomagnetic activity, with most studies focusing on geostationary orbit or beyond [e.g., *Johnson et al.*, 1975; *Geiss et al.*, 1979; *Johnson*, 1979; *Lennartsson et al.*, 1981; *Young*, 1983; *Fu et al.*, 2001]. ISEE-1 density data from 0.1 to 17 keV showed that the O^+/H^+ ratio during disturbed conditions decreased from L = 4–6 but increased from L = 6–12 [*Lennartsson and Sharp*, 1982]. At geostationary orbit, ESA/GEOS 1 and 2 observed an increase in the 0.9–16 keV O^+/H^+ ratio with increasing Kp [*Young et al.*, 1982]. At 7–8 R_E and 15–20 R_E, Cluster/CODIF partial density data from 1 to 40 keV were used to characterize inner magnetospheric composition. In the midtail region, the O^+/H^+ ratio increased with increasing Kp for all values of F10.7 [*Maggiolo and Kistler*, 2014], while near geostationary orbit the ratio of O^+/H^+ generally increased with Kp although these enhancements were strongly dependent on MLT [*Kistler and Mouikis*, 2016]. At higher energies (~20–315 keV), the O^+/H^+ ratio was found to increase during disturbed conditions, both from 3–7 R_E and 28–226 keV at 15 R_E [*Gloeckler and Hamilton*, 1987]. Observations at geosynchronous orbit by the LANL-Geo MPA instruments, which do not have explicit composition capability, have been used to infer the Kp dependence of nightside plasma sheet composition over a full solar cycle [*Denton et al.*, 2005].

The NASA Van Allen Probes (formerly Radiation Belt Storm Probes, RBSP) mission [*Mauk et al.*, 2013] was designed to acquire the most comprehensive, definitive measurements of waves and particles ever conducted inside of geostationary orbit. The Helium-Oxygen-Proton-Electron (HOPE) mass spectrometers [*Funsten et al.*, 2013] on each Van Allen Probe were specifically designed to minimize the backgrounds induced by penetrating radiation that have contaminated previous measurements in the radiation belts.

This study is a statistical characterization and survey of the plasma environment inside geostationary orbit, from L = 2–6. We present electron and ion measurements from 0.1 to 30 keV acquired by the identical HOPE-A and HOPE-B mass spectrometers on board the two Van Allen Probes spacecraft. We combine measurements from both spacecraft and focus on global distributions of electron flux and species-resolved ion fluxes of H^+, He^+, and O^+, as well as ion abundances as a function of L shell and MLT (magnetic local time). We examine the effects of geomagnetic activity on flux levels and relative abundances by subdividing the data based on the Kp index. We describe the electron and ion fluxes in the context of our current understanding of inner magnetosphere dynamics.

2. Instrumentation and Data Analysis

The observations used in this study are from the HOPE mass spectrometers [*Funsten et al.*, 2013], which are part of the Energetic particle, Composition and Thermal plasma (ECT) instrument suite [*Spence et al.*, 2013] on NASA's Van Allen Probes mission [*Mauk et al.*, 2013]. Two identically instrumented spacecraft comprise the Van Allen Probes. Each spacecraft orbit has an apogee of 5.8 R_E, a perigee of ~620 km, and an inclination of ~10°. The orbits of the two spacecraft precess at a rate of about 210° per year, allowing for full MLT coverage every ~1.7 years.

Each HOPE mass spectrometer alternately measures electrons and ions in 72 energy steps with energy resolution ΔE/E ~ 15%, covering an electron energy range 15 eV to ~50 keV and ion energy range 1 eV/q to ~50 keV/q, where q is the ion charge. To simplify operations, HOPE measurements are not synchronized with the spacecraft spin [*Funsten et al.*, 2013]. A full ion or electron measurement is made every ~11 s, covering ~375° of spacecraft spin divided into 16 spin-angle sectors. Ions and electrons are measured using time-of-flight to reject events generated in the detector subsystem by penetrating background and, for ions, to obtain ion mass (H^+, He^+, and O^+). The instantaneous HOPE polar angle field of view is fan shaped and spans 180° across five equally sized pixels, while the instantaneous azimuthal field of view is 4.5°. Spacecraft spin sweeps the HOPE aperture through the full 360° range of azimuthal angles.

Reduction of background counts in HOPE by penetrating radiation is achieved by a combination of shielding and coincidence measurement (through time-of-flight) of plasma ions and electrons that enter the detector subsystem. Background count rates from penetrating radiation are negligible in all regions except in the inner zone, where the random coincidence event rate from penetrating protons, which are identified using regularly reported time-of-flight spectra, can be comparable to the lowest measured event rates from plasma particles during these intervals. This study examines L ≥ 2, which lies outside this region. For this survey, we use the ECT Release 3 data from both the A and B Probes [https://rbsp-ect.lanl.gov], which accounts for the time-dependent variation in absolute detection efficiency of the channel electron multiplier (CEM) detectors that is enabled by comparison of coincident and noncoincident event rates [*Funsten et al.*, 2005]. To facilitate analysis of data over time, a uniform data product has been created using the omnidirectional flux as a function of species, energy, and time. The ECT Release 3 data used in this study range from 26 October 2012 to 29 February 2016. For convenience in capturing the character and dynamics of the different plasma populations, each ion or electron measurement was linearly interpolated onto a fixed energy grid at energies 0.03, 0.1, 0.3, 1, 3, 10, and 30 keV. The data were then resampled into 3 min mean fluxes to increase the precision of measured flux by a factor of ~2.9 relative to a single, complete ion or electron measurement that is acquired every two spins (~21.8 s). The spacecraft traverses a maximum of 0.2 L over a 3 min integration interval, with substantially smaller distances near apogee. The observations presented here are minimally affected by spacecraft charging [*Sarno-Smith et al.*, 2016]. The resulting data set contains a total of 749,824 measurements combined from HOPE-A and HOPE-B. This data set also includes ephemeris, *Kp* index, and supporting information; thus, the data can be selected or further combined according to geomagnetic activity, time, MLT, and L shell.

3. Observations

In the 3.3 years of data utilized in this survey, the Van Allen Probes spacecraft spatial coverage spanned nearly two full orbital precessions and thus complete sampling over the full near-equatorial plane. Here we present data at 0.1, 1, and 10 keV. (Plots for the other energies are provided in the supporting information.) The dynamics of the 0.1 keV population are dominated by electric field drifts (i.e., $E \times B$ drift) [*Friedel et al.*, 2001]. The dynamics of the populations sampled at 10 keV are generally dominated by magnetic field drifts—predominantly gradient-curvature drifts. The 1 keV channel samples the intermediate population whose dynamics are governed by both $E \times B$ and gradient-curvature drifts. As shown in the supporting information, all observed 0.3 and 3 keV flux distributions are comparable to the 1 keV flux distributions, indicating that electric field drift processes transition from a primary to secondary effect between 3 and 10 keV for the average geomagnetic conditions over the course of this study.

Fluxes are sorted into (L and MLT) bins from L = 2 to L = 6 with 0.25 L and 0.5 h MLT resolution. In each bin, median flux values are calculated from the 3 min mean samples. All data utilized in this study are subdivided by precessional pass: Precession 1 spans October 2012–July 2014 and Precession 2 spans August 2014 to
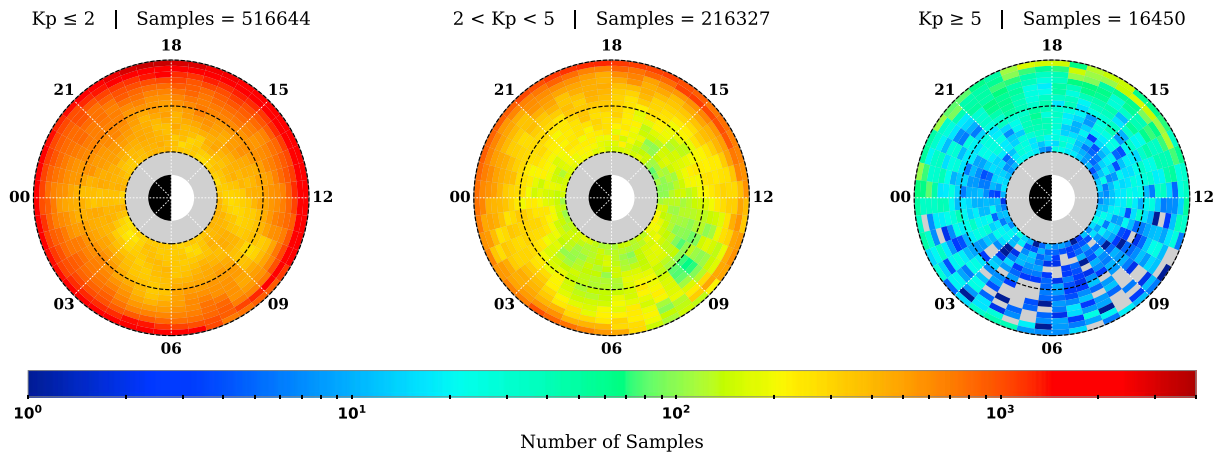
Figure 2. Number of 3 min samples collected in each L-MLT bin. L values range from L = 2 (interior dashed circle) to L = 6 (exterior solid circle). The total number of samples for each species is 749,824. These samples are organized by *Kp*: quiet time (left: *Kp* ≤ 2); moderate activity (middle: 2 < *Kp* < 5; and active (right: *Kp* ≥ 5). Satellite apogee is evident with the enhanced number of samples beyond L ~ 5.5. Pixels with no 3 min samples are represented in grey.

February 2016. We observe only subtle differences in specific features between the data of Precession 1 and Precession 2 and thus combine these to derive general observations consistent across both precessional passes. For this near-equatorial inner magnetosphere study, L is computed using the OP77 magnetic field model for locally mirroring particles [*Olson and Pfitzer*, 1977]. Use of OP77 is the COSPAR PRBEM (Committee on Space Research Panel for Radiation Belt Environment Modeling) standard, and its application in this region is supported by phase space density matching [*Morley et al.*, 2013]. The data are further categorized by the geomagnetic activity index *Kp*. This index is an excellent proxy for convection [*Thomsen*, 2004], which in turn controls the particle drift orbits in the inner magnetosphere at the energies measured by HOPE [*Korth et al.*, 1999]. Figure 2 shows the number of 3 min samples in each (L and MLT) bin for *Kp* ≤ 2, 2 < *Kp* < 5, and *Kp* ≥ 5. For *Kp* ≤ 2, all (L and MLT) bins have at least 200 samples, and the decreasing number of samples with increasing activity reflects the overall occurrence rates of various levels of *Kp* in the current quiet solar cycle.

The median omnidirectional differential number fluxes for electrons (e^-), H^+, He^+, and O^+ are shown in Figures 3–6, respectively. In the individual polar plots, the Sun is to the right and L shell coverage spans from L = 2–6. Each column in these figures represents a single energy channel (0.1, 1, and 10 keV from left to right). Each row represents a level of geomagnetic activity, with quiet activity (*Kp* ≤ 2) at the top, moderate activity (2 < *Kp* < 5) in the middle, and active times (*Kp* ≥ 5) at the bottom.

These flux plots include the open drift path boundary, shown as a pink line overlaid on a white line. The open drift path boundary is the location on the UBK access map (e.g., Figures 1i and 1j) where the access region transitions from open to closed or banana orbits. The open drift path boundary for each panel (Figures 3–6) is obtained from UBK access maps for the corresponding energy and geomagnetic activity level and depends on both of these quantities. The values of *Kp* used in calculating the boundary for quiet, moderate, and active times were 1.0, 3.0, and 5.3, respectively. These values correspond to the median value of *Kp* during the defined levels of activity. During geomagnetically active times, the boundary moves Earthward. For ions at higher energies the boundary moves Earthward until its shape drastically changes as the particle trajectories transition from electric field dominated to magnetic field dominated.

3.1. Electrons

Figure 3 shows the global distribution of the median electron flux. Each energy channel (column) has a log-space colorbar which covers 2.1 orders of magnitude, allowing direct comparison of flux magnitudes across different levels of geomagnetic activity. For ease of identifying spatial and temporal changes, the colorbars are qualitatively partitioned into flux ranges of comparatively low (~blue), moderate (~green), and high (~red) flux magnitudes. For 0.1 keV electrons, we define the low and high flux ranges as $<10^7$ and $>10^8$ cm^{-2} s^{-1} sr^{-1} keV^{-1}, respectively; for 1 keV electrons, low and high fluxes correspond to $<2 \times 10^6$,
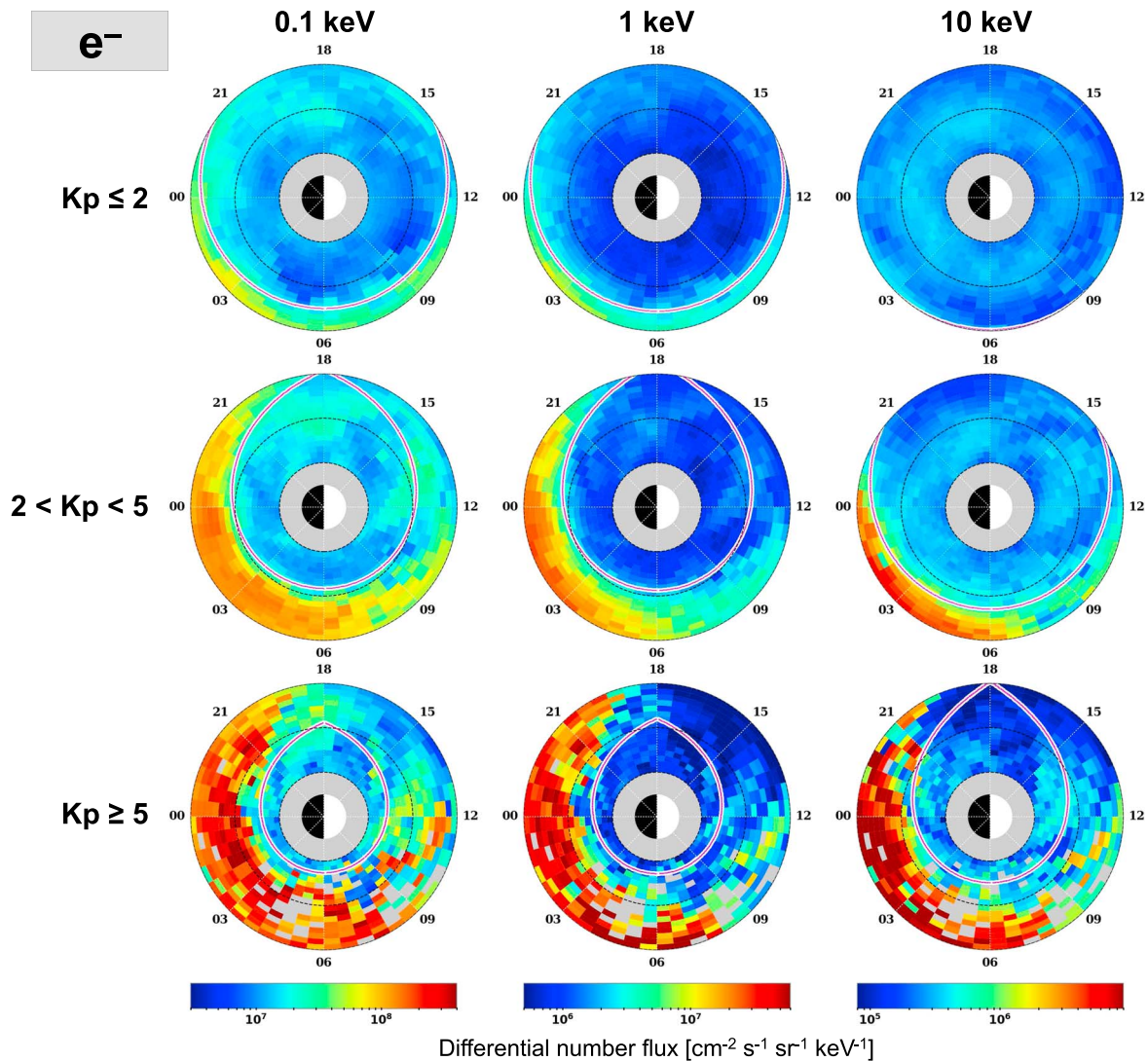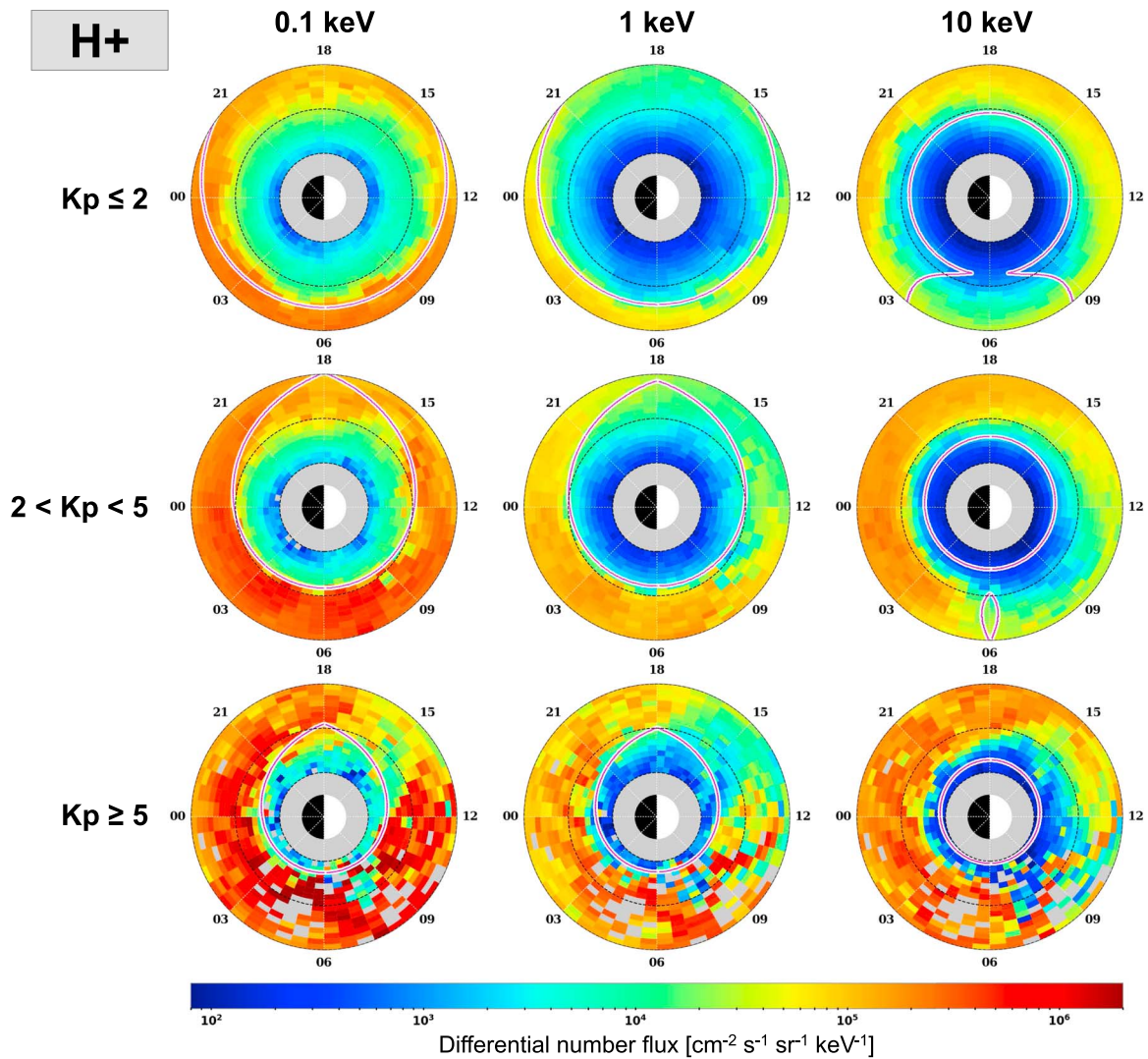
Figure 3. Median omnidirectional electron differential flux as a function of L and MLT for $2 \leq L \leq 6$. The Sun is to the right. Dashed circles show L = 2, 4, and 6. Columns from left to right represent energy channels: 0.1, 1, and 10 keV, respectively. Rows represent geomagnetic activity: the top row is low activity ($Kp \leq 2$), the middle row is moderate activity ($2 < Kp < 5$), and the bottom row is active times ($Kp \geq 5$). The open drift path boundary, defined from the UBK access maps as the region where access transitions from open to closed/banana orbits, is shown as a pink line overlaid on a white line. Each energy channel has its own colorbar showing the flux magnitude, with grey pixels representing regions with no data.

and $>10^7$ cm^{-2} s^{-1} sr^{-1} keV^{-1}, respectively; and for 10 keV electrons, low and high fluxes are defined as $<3 \times 10^5$ and $>2 \times 10^6$ cm^{-2} s^{-1} sr^{-1} keV^{-1}, respectively. At each energy, the moderate flux range lies between the low and high flux ranges.

The median electron flux increases with increasing geomagnetic activity in all three energy channels. Further, during more geomagnetically active times the regions of enhanced electron flux expand to lower L. For example, in the 0.1 keV channel (left column), moderate fluxes are observed only beyond L = 5.5 during quiet times. Regions of enhanced flux are found as far inward as L = 4.25 during moderate activity, and to L = 3.5 during active times. A similar trend occurs in the 1 and 10 keV channels.

The electron flux is strongly energy dependent, with the largest electron fluxes observed at 0.1 keV and the smallest fluxes at 10 keV. Lower energy electrons penetrate to lower L shell than higher energy electrons for a given geomagnetic activity level. Examining Figure 3 (bottom row), the largest 0.1 keV fluxes are observed at L = 3 whereas the largest 10 keV fluxes are confined to $L \geq 4$. The distribution of high fluxes in local time is weakly energy dependent, with regions of enhanced fluxes observed in the postmidnight and dawn
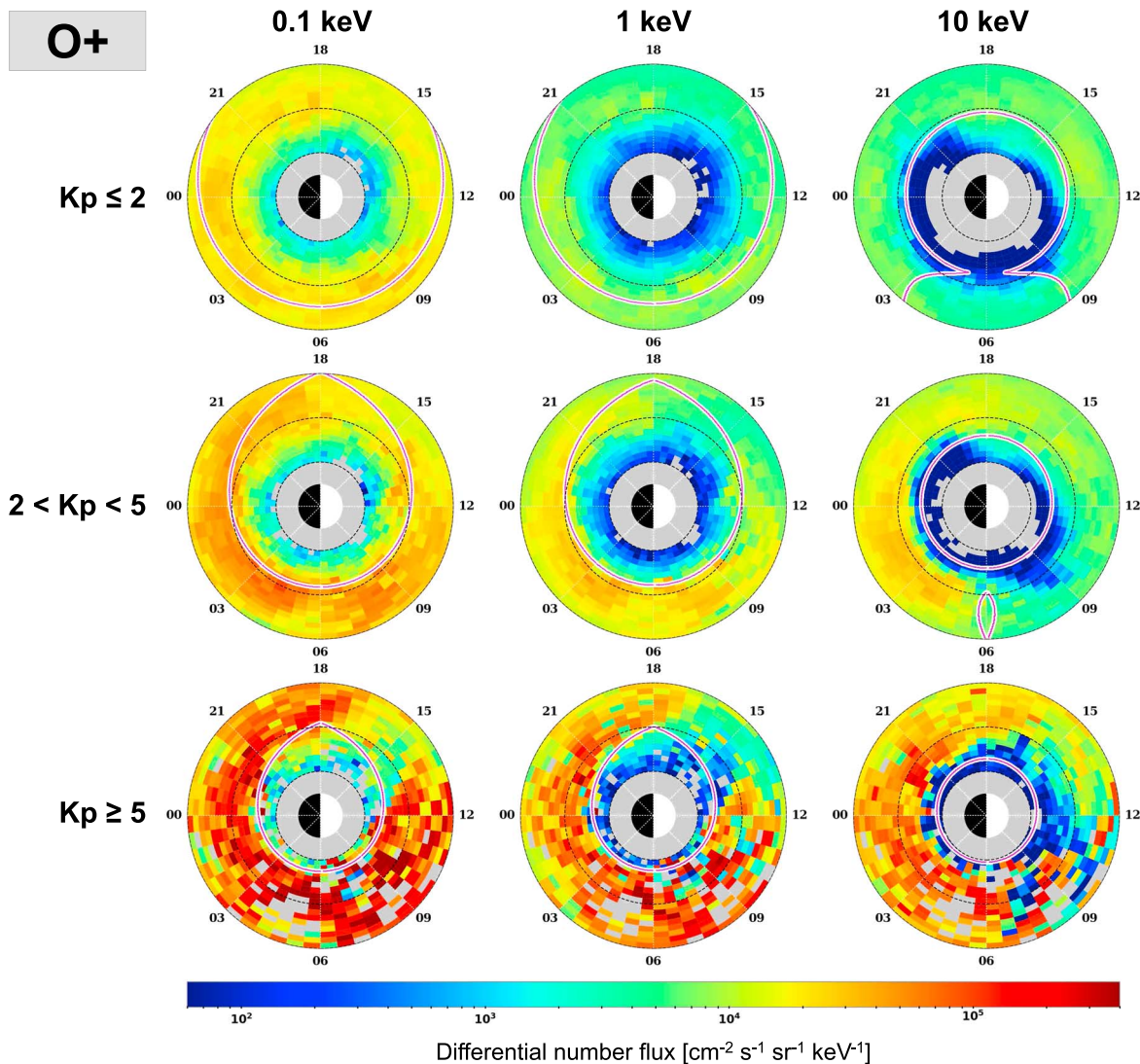
Figure 4. Median omnidirectional proton differential flux as a function of L and MLT for $2 \leq L \leq 6$ in the same format as Figure 3. A common flux colorbar is used for all panels.

sectors for all energy channels and geomagnetic activity levels. However, these regions of enhanced fluxes at lower energy span a broader range of MLT relative to the MLT coverage of the high-energy populations. For example, during moderate activity (middle row), the western edge of this region of enhancement is near 2100 MLT at 0.1 keV and shifts to midnight at 10 keV.

3.2. Hydrogen

Figure 4 shows the global distribution of the median proton flux. Protons show less dynamic range across different energies than electrons so panels in this figure share a single colorbar allowing for direct comparison of fluxes across all energies and activity levels. As with electrons, the colorbar is qualitatively partitioned into flux ranges of comparatively low (~blue, $<2 \times 10^3$ cm^{-2} s^{-1} sr^{-1} keV^{-1}) and high (~red, $>8 \times 10^4$ cm^{-2} s^{-1} sr^{-1} keV^{-1}) flux, with the moderate flux range (~green) in between the low and high flux ranges. Proton flux in the 0.1 keV channel is greater than the flux in the 1 or 10 keV channels, while higher proton flux is observed at 10 keV than at 1 keV. The global proton flux increases with increasing geomagnetic activity. Further, during more geomagnetically active times the regions of high proton flux expand to lower L. This is illustrated in the 0.1 keV channel (left column), in which high fluxes are limited to L shells greater than 4.25 during quiet times. These regions of enhanced fluxes extend as low as L = 3.5 during moderate activity, and to L = 2.5 during active times. A similar trend occurs in both the 1 and 10 keV channels.

Figure 5. Median omnidirectional O$^+$ differential flux as a function of L and MLT for $2 \leq L \leq 6$ in the same format as Figure 3. A common flux colorbar is used for all panels.

The spatial distributions of proton flux exhibit a strong energy dependence. At 0.1 keV (left column), during quiet times enhanced fluxes are observed at all MLT, with more flux observed in the dawn hemisphere extending from ~0000 to 1200 MLT. These larger fluxes in the dawn hemisphere are consistent with the open trajectory boundary shown with the white/pink line. These fluxes extend down to L = 4.25 except in the early afternoon sector where these fluxes are limited to L ≥ 4.5. During moderate activity, proton fluxes at 0.1 keV cover all MLT, with the largest fluxes extending down to L = 3.75 from premidnight through dawn and into the morning, consistent with the open trajectory boundary obtained from the UBK formalism. In the afternoon sector, fluxes are smaller and are limited to larger L shell than at other MLT. During active times, in the 0.1 keV channel the observed fluxes are again consistent with the open trajectory boundary; additionally, there is a distinct gap in the proton flux near 1500 MLT.

In contrast, during quiet times, high proton fluxes at 1 keV are limited to the nightside and morning sectors and L ≥ 5. With increasing geomagnetic activity, these high fluxes extend to lower L shell and the westward edge of the enhancement region extends from midnight into the premidnight sector. During active times, the westward expansion of the boundary and extension to lower L shell is further enhanced, and the eastward boundary extends through the morning sector to early afternoon. These observations are generally consistent with the open trajectory boundaries extracted from the UBK access map models.
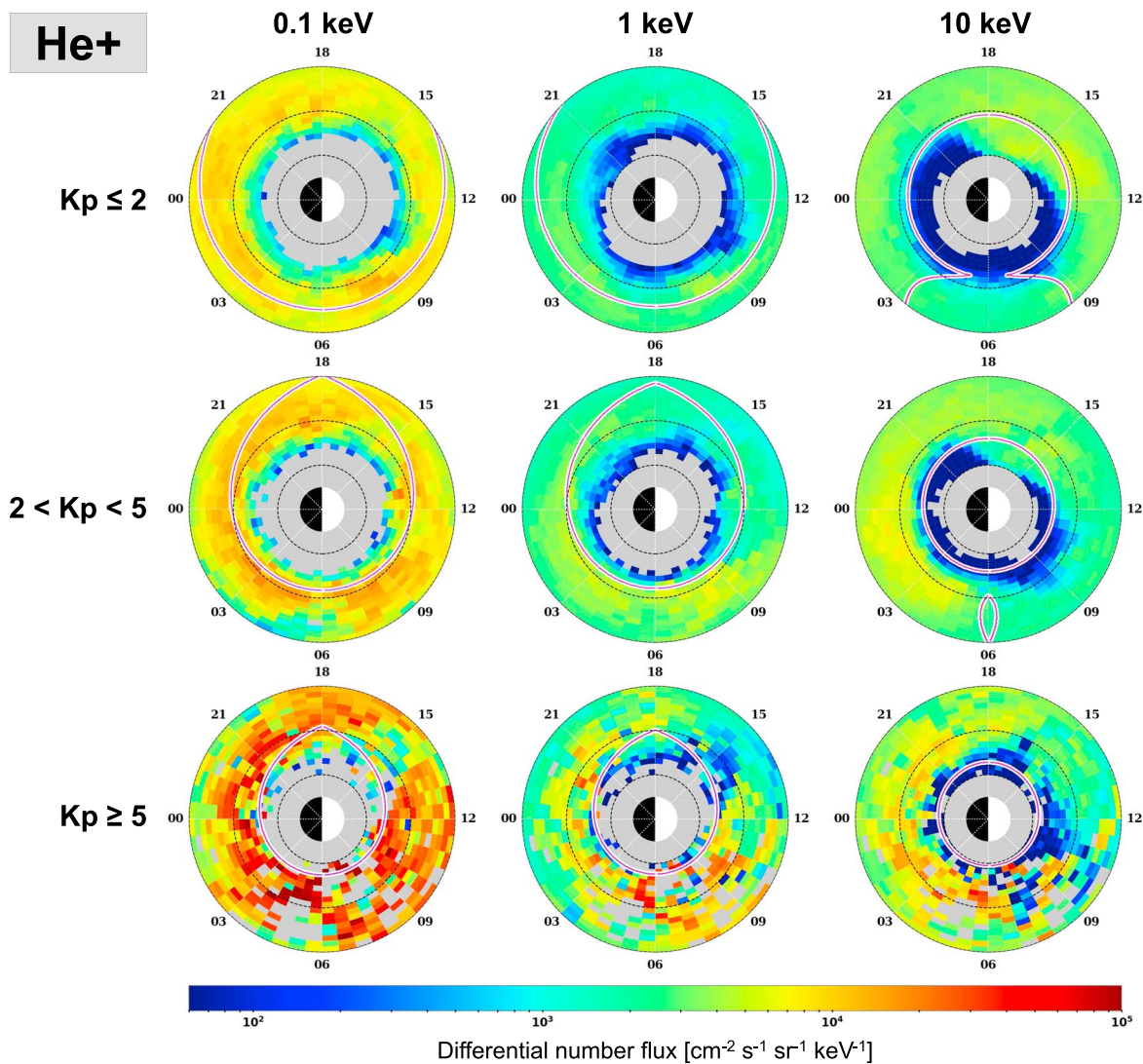
Figure 6. Median omnidirectional He$^+$ differential flux as a function of L and MLT for $2 \leq L \leq 6$ in the same format as Figure 3. A common flux colorbar is used for all panels.

A distinct change in the local time distribution of enhanced fluxes occurs at 10 keV. There is a depletion observed prenoon which is more apparent at 10 keV than at lower energies. During quiet times, enhanced fluxes extend from midnight westward into the evening and afternoon sectors. Increasing geomagnetic activity extends these fluxes to lower L shell and extends the eastward boundary into the postmidnight and dawn sectors.

3.3. Oxygen

Figure 5 shows the global distribution of the median O$^+$ flux. All panels in this figure again share a single colorbar. As with protons, the colorbar is qualitatively partitioned into flux ranges of comparatively low (~blue, $<10^3$ cm^{-2} s^{-1} sr^{-1} keV^{-1}) and high (~red, $>2 \times 10^4$ cm^{-2} s^{-1} sr^{-1} keV^{-1}) flux, with the moderate flux range (~green) in between the low and high flux ranges. More O$^+$ flux is seen at lower energies than at higher energies. During geomagnetically active times, the global O$^+$ flux increases and the regions of high O$^+$ flux expand to lower L, consistent with open access boundary obtained from the UBK modeling. At 0.1 and 1 keV during quiet times, the O$^+$ flux is nearly uniform in MLT with a gap at 1500 MLT. These fluxes are moderate at 1 keV and moderate to high at 0.1 keV. During moderate and active times, the western edge of the high flux region lies near dusk at these energies. This enhanced flux region extends eastward, through the
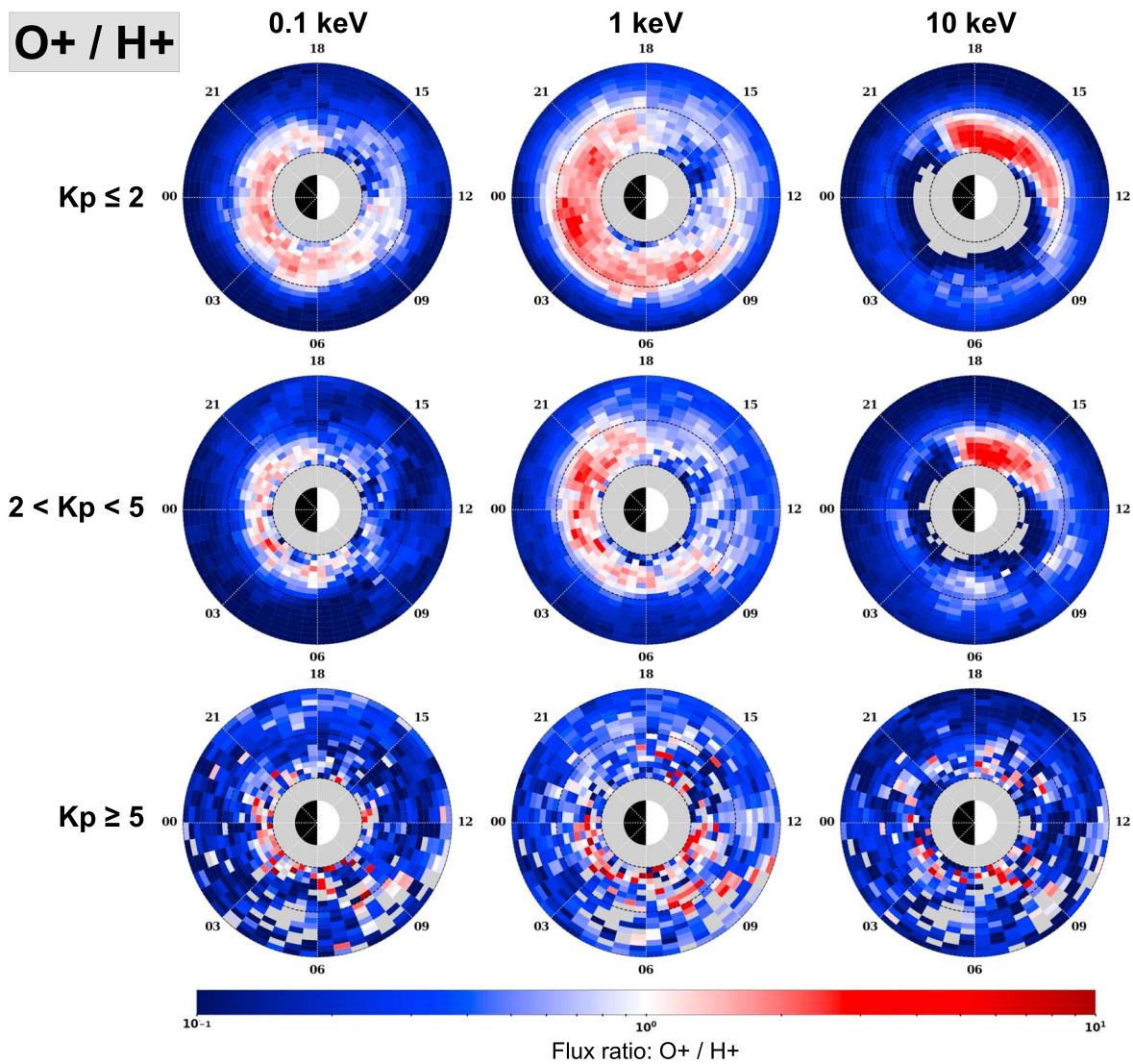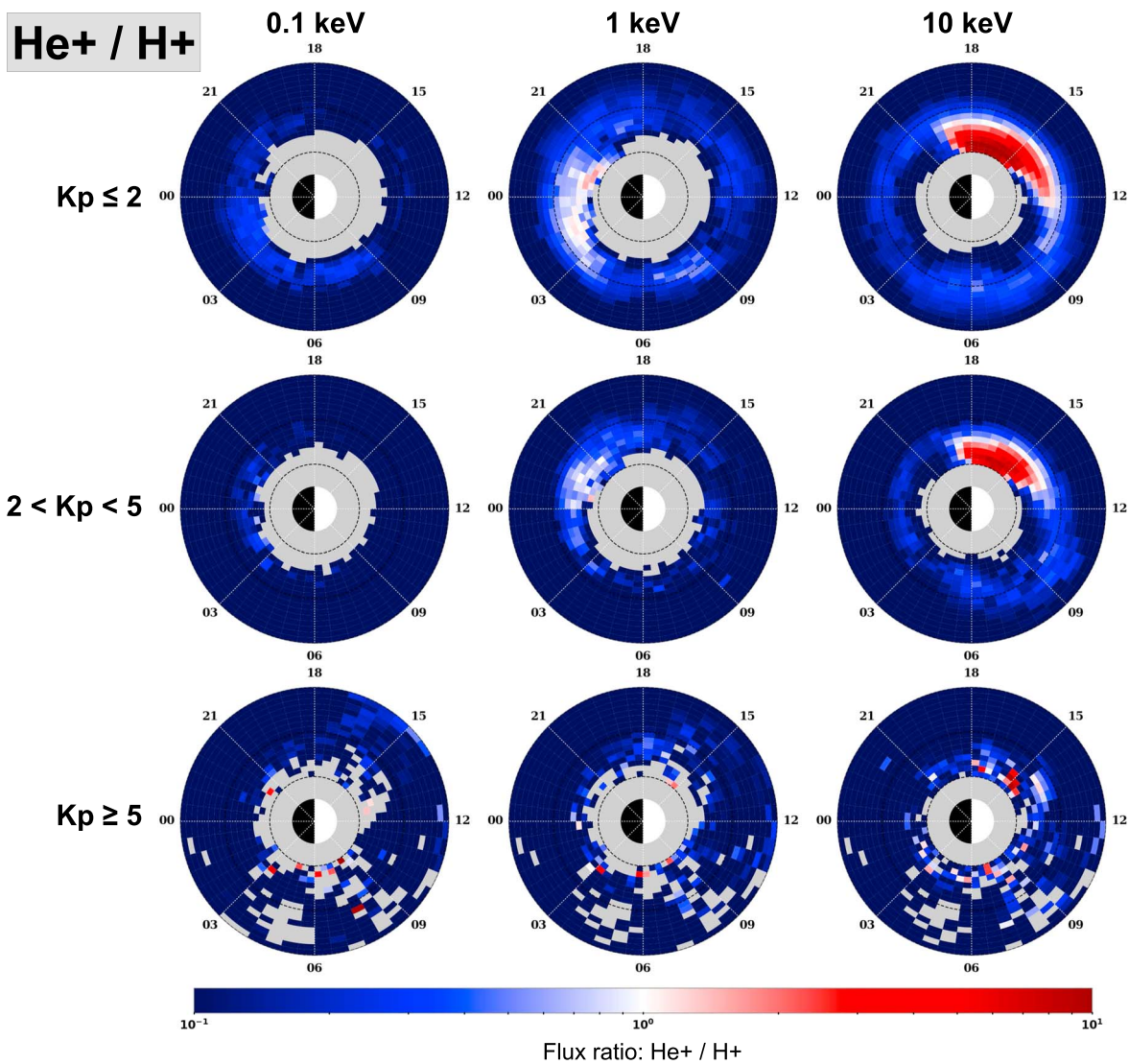
Figure 7. : Ratio of O^+ to H^+ flux as a function of L and MLT for $2 \leq L \leq 6$ in the same format as Figure 3. Red indicates O^+ dominance, blue indicates H^+ dominance, and white indicates similar abundances of O^+ and H^+. At 10 keV, O^+ dominates in the afternoon/dusk sectors during quiet and moderate activity.

midnight and dawn sectors with the eastern edge lying near noon for the 0.1 keV population and near 0900 MLT for the 1 keV population. At 10 keV, high fluxes are observed in the premidnight and postmidnight sectors during moderate and active times. At 10 keV during quiet times, moderate fluxes are observed for $L \geq 4$ at all MLT, with predominantly low fluxes inside $L = 4$. The L and MLT structure of these fluxes is generally consistent with the open trajectory boundary; deviations between observations and UBK modeling will be addressed in section 4.

A striking feature is observed at 10 keV during quiet and moderate activity: moderate O^+ fluxes extend down to $L = 2$ in the afternoon sector. This "afternoon bulge" feature in the O^+ flux is persistent across multiple orbits spanning both precessional passes of the spacecraft. When displaying the data using smaller gradations of Kp the feature is distinct for $Kp \leq 4$ (not shown). The O^+ abundance relative to other species in this region is discussed in section 3.5.

3.4. Helium

Figure 6 shows the global distribution of the median He^+ flux. As with protons, the colorbar is qualitatively partitioned into flux ranges of comparatively low (~blue, $<8 \times 10^2$ cm^{-2} s^{-1} sr^{-1} keV^{-1}) and high (~red, $>9 \times 10^3$ cm^{-2} s^{-1} sr^{-1} keV^{-1}) flux, with the moderate flux range (~green) in between the low and high
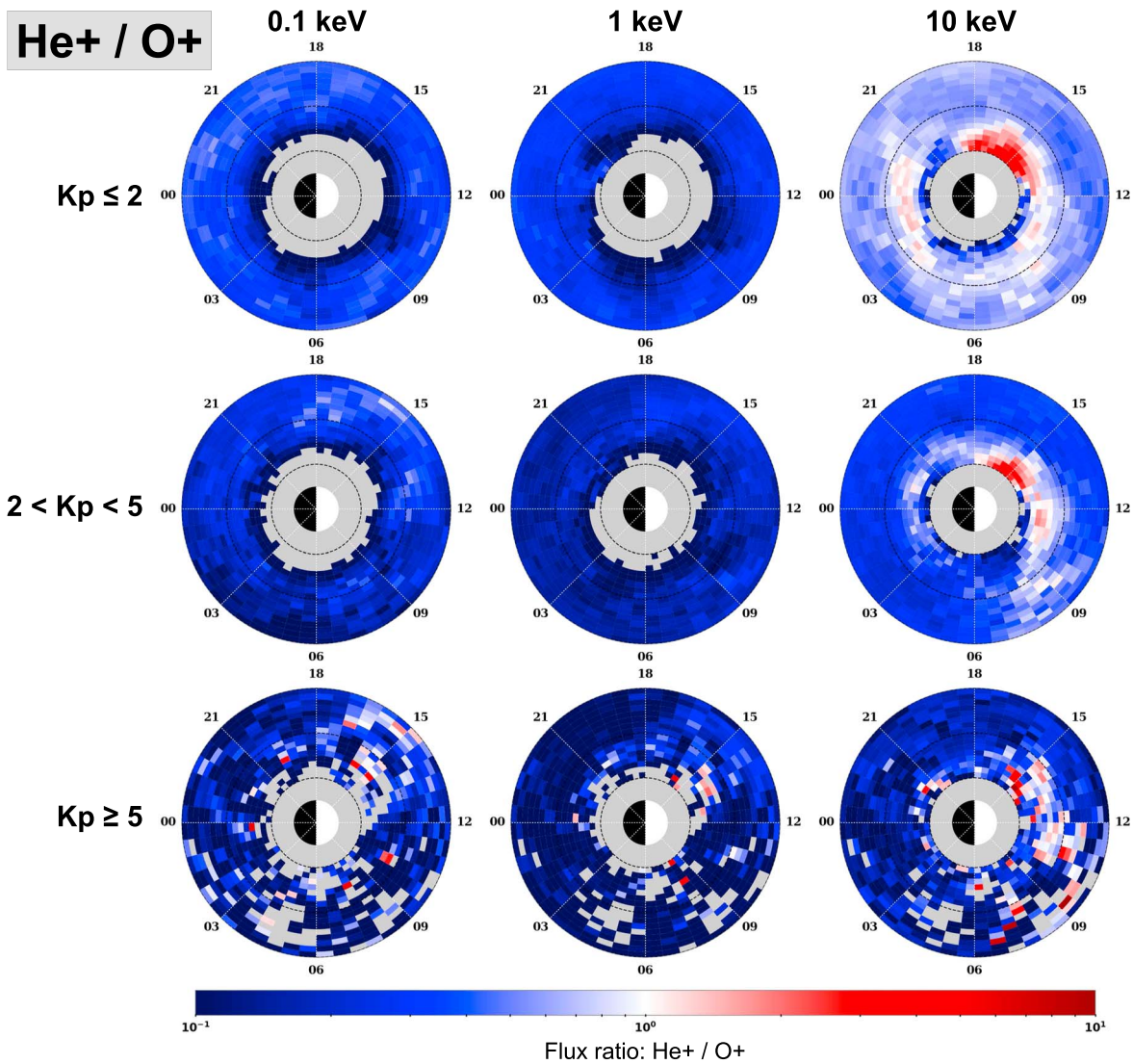
Figure 8. Ratio of He$^+$ to H$^+$ flux to as a function of L and MLT in the same format as Figure 3. Red indicates He$^+$ dominance, blue indicates H$^+$ dominance, and white indicates similar abundances of He$^+$ and H$^+$. At 10 keV, He$^+$ dominates in the afternoon/dusk sectors during quiet and moderate activity.

flux ranges. The largest He$^+$ fluxes are in the 0.1 keV channel, while the magnitudes of fluxes observed at 1 and 10 keV are similar, with slightly more flux in the highest energy channel. As with the other species, as *Kp* increases, the global He$^+$ flux increases and larger fluxes penetrate to lower L shells, consistent with the open trajectory boundaries. At 0.1 keV, high fluxes are found at all MLT with a minimum at 1500 MLT. At 1 keV, moderate flux is observed at all MLT with a very slight flux enhancement region in the morning sector. At 10 keV, moderate fluxes are found at all MLT, with slight flux enhancements in the afternoon sector during quiet times and in the premidnight and postmidnight sectors during moderate and active times.

Even more prominent than for O$^+$, the so-called afternoon bulge is clearly apparent in 10 keV He$^+$ during both quiet and moderate activity. The He$^+$ afternoon bulge extends down to L = 2 and is centered at 1700 MLT. As with the O$^+$ afternoon bulge, the He$^+$ bulge is persistent across both precessional passes of the two spacecraft.

3.5. Ion Abundance Ratios

In order to compare the relative abundances of the ion species, we present ratios of the median fluxes. Figures 7–9, respectively, show the O$^+$/H$^+$, He$^+$/H$^+$, and He$^+$/O$^+$ abundance ratios on the same logarithmic scale. These ratios are calculated for each 3 min sample. The ratios are then binned by L and MLT. Next,

Figure 9. Ratio of He$^+$ to O$^+$ flux to as a function of L and MLT in the same format as Figure 4. Red indicates He$^+$ dominance, blue indicates O$^+$ dominance, and white indicates similar abundances of He$^+$ and O$^+$. The afternoon bulge observed at 10 keV is predominantly He$^+$.

the median flux ratio for each L-MLT bin is calculated from the 3 min ratio samples, and finally, the results are sorted by *Kp*. Following the format of previous figures, each column represents an energy channel (0.1, 1, and 10 keV, respectively, from left to right) and each row a range of geomagnetic activity, ranging from quiet (top) to moderate (middle) to active (bottom). The colorbars on these figures are identical and range from 0.1 to 10. As with the flux distributions, the 3 keV abundance ratios are comparable to the 1 keV distributions (see supporting information).

Figure 7 shows the ratio of O$^+$ to H$^+$ fluxes. Red indicates O$^+$ dominance, blue indicates H$^+$ dominance, and white represents similar abundances of O$^+$ and H$^+$. During quiet and moderate activity, O$^+$ generally dominates at low L with strong MLT dependence. The oxygen-dominated region extends farthest out during quiet times, to L = 4.25. With increasing geomagnetic activity, this outer boundary moves inward to smaller L. At active times (bottom row, *Kp* ≥ 5), the inner magnetosphere is proton dominant (on average) during active times, with the exception from L = 2–4 at energies ≥10 keV. The O$^+$ abundance is featureless, though minimal counts in the morning sector inhibit assessment of the O$^+$ abundance structure.

The region of O$^+$ dominance is strongly energy dependent. At 0.1 and 1 keV during quiet and moderate activity, the westward boundary of this feature lies near dusk. The enhancement in O$^+$ abundance extends
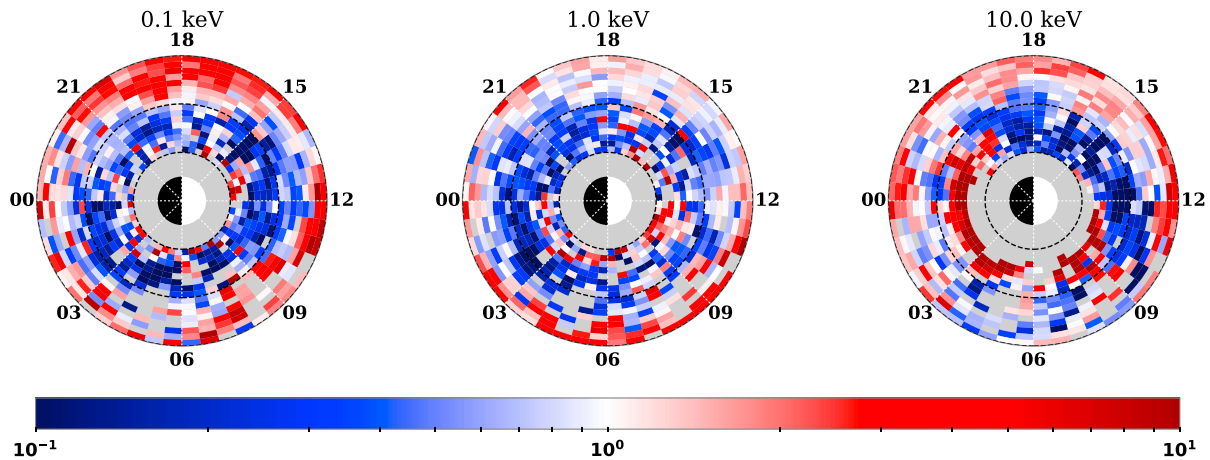
Figure 10. Ratio of O^+/H^+ flux at $Kp \geq 5$ to the O^+/H^+ flux at $Kp \leq 2$. The Sun is to the right. Dashed circles show L = 2, 4, and 6. Panels from left to right represent energy channels: 0.1, 1, and 10 keV, respectively. Red indicates an increase in the O^+/H^+ flux during geomagnetically active times; blue indicates a decrease in the O^+/H^+ flux during active times, and white indicates that the O^+/H^+ flux ratio remains approximately constant regardless of geomagnetic activity.

eastward through the night and morning sectors, with the eastern boundary lying near 0900 MLT. A depletion of O^+/H^+ flux is observed in the afternoon sector, in the region of the afternoon bulge seen at higher energies. At 10 keV the O^+ afternoon bulge is prominent, extending from 1100 to 2000 MLT. The bulge is broader in MLT during quiet times and disappears altogether for $Kp \geq 5$. The bulge is not present at 3 or 30 keV (see supporting information).

Figure 8 shows the ratio of fluxes of He^+ to H^+. Red represents He^+ dominance, blue represents H^+ dominance, and white represents similar abundances of He^+ and H^+. Protons generally dominate although significant He^+ is present during quiet and moderate geomagnetic activity. At 0.1 keV protons dominate, though at $L < 4$ significant He^+ is present on the nightside and morning sectors during quiet times and in the nightside only during moderate activity. At 1 keV, similar abundances of He^+ and H^+ are observed near midnight during quiet and moderate activity. This He^+ is restricted to $L < 4$; 1 keV He^+ is also observed at other MLT though not in any substantial amount. At 10 keV during quiet and moderate activity, a strong preponderance of He^+ comprises the afternoon bulge, dominating the protons by a factor of 10. As with the O^+ afternoon bulge, the He^+ bulge spans a broader range of MLT during quiet times. The bulge is not present at 3 or 30 keV (see supporting information).

Figure 9 shows the ratio of fluxes of He^+ to O^+. Red indicates He^+ dominance, blue indicates O^+ dominance, and white represents equal abundances of He^+ and O^+. These observations show that at 0.1 and 1 keV, O^+ is the dominant species. However, the 10 keV afternoon bulge is He^+ dominant. Additionally, a significant proportion of 10 keV He^+ is present on the nightside during low and moderate activity, and He^+ and O^+ are found in near-equal abundances throughout much of the inner magnetosphere.

Figure 10 shows the L-MLT-energy dependence of changes in the O^+/H^+ flux ratio with Kp. The colorbar represents the ratio of O^+/H^+ flux at $Kp \geq 5$ to the O^+/H^+ flux at $Kp \leq 2$. Red indicates an increase in the O^+/H^+ flux and blue a decrease in the O^+/H^+ flux during geomagnetically active times. White indicates that the O^+/H^+ flux ratio remains approximately constant regardless of geomagnetic activity. Across all energies, the O^+/H^+ ratio generally increases near L = 5–6, with the exception of 0300–0900 MLT for energies $\geq$10 keV. In contrast, at $L < 5$ the O^+/H^+ flux ratio at all energies was generally higher during quiet times than geomagnetically active times. The primary exception is from 2100 to 1200 MLT for energies $\geq$10 keV.

4. Discussion

The electron, H^+, O^+, and He^+ omnidirectional fluxes depend on geomagnetic activity, L shell, local time, particle species, and energy. In this section, we discuss these observations in the context of our understanding of plasma sheet access to the inner magnetosphere, the physics underlying the various source and loss

mechanisms in this region, and the dynamics which govern how these distributions evolve in time. Plasma sheet access is characterized using the UBK ion access maps discussed in section 1 and shown in Figure 1. Our UBK analysis is limited to the equatorial plane ($K = 0$) which matches the near-equatorial orbit of the Van Allen probes and our assumption of equatorially mirroring particles. Additionally, our implementation of UBK uses a dipole magnetic field, a reasonable assumption within L = 6, and a Volland-Stern electric field model. This time-stationary electric field is an appropriate reference against which we compare our average particle flux statistics.

4.1. Access

The L shell and MLT dependence of the electron and ion fluxes were shown in Figures 3–6. Both electron and ion fluxes are larger at lower energies than at higher energies; this is attributed to the plasma sheet, which is the source for these particles and has a similar energy distribution. For a given geomagnetic activity level, the highest electron fluxes extend to lower L shells at lower energies. For ions, the highest fluxes tend to penetrate to similar L shells independent of energy. These observations are consistent with the energy dependence of the open trajectory boundaries overlaid on the flux distributions.

For electrons and all three ion species, regions of highest flux extend to lower L shell with increasing geomagnetic activity. Similarly, the fluxes increase with increasing geomagnetic activity for all energies and species (Figures 3–6). For lower energies, the observations are consistent with stronger convection electric fields that push the Alfvén layer Earthward, allowing enhanced fluxes of electrons and ions from the plasma sheet to be observed at lower L shells. At higher energies, the deeper penetration of the substorm injection boundary and enhanced convection both likely play a role.

Earth's corotation electric field and the gradient-curvature drifts deflect electrons in the same direction (eastward or toward dawn); therefore, it is expected that the spatial distribution in MLT of electron fluxes will be similar for all energies. The observed distribution of enhanced electron fluxes in MLT shows minimal energy dependence (Figure 3), consistent with the expected drift trajectories. Regions of high electron flux extend into the premidnight sector for larger Kp, consistent with the Alfvén layer moving Earthward during active times. This western edge of the enhancement region is influenced by the energy-dependent Alfvén layer, which restricts the MLT access of the higher energy electrons.

In contrast to the electrons, the distributions of enhanced ion fluxes in MLT depend strongly on energy and Kp (see Figure 1 of this study and *Korth et al.* [1999], Figure 2). Ion dynamics at ~10–100 eV are dominated by the electric field drifts resulting from a superposition of the corotation field and the dawn-dusk cross-tail field. These electric fields inject plasma sheet ions into the inner magnetosphere near midnight/premidnight and drive those ions eastward, from dawn to noon and into the evening sector. The open trajectory boundary is strongly dependent on energy and Kp. This boundary layer lies at larger L for higher energy particles, which inhibits access of higher energy ions to the lowest L shells. The 0.1 keV distributions of H^+, O^+, and He^+ (Figures 4–6) are consistent with ions on open drift paths.

For all observed ion species, the MLT distributions for the 1 keV and 3 keV (see supporting information) populations are more similar to the 0.1 keV than to the 10 keV populations, particularly during quiet and moderate activity. These observations indicate that the dynamics of the 1 keV (and the 0.3 and 3 keV) ion populations are primarily driven by electric field drifts, similar to the 0.1 keV populations. Furthermore, this indicates that the global transition to magnetic field drifts as the dominant mechanism occurs between 3 and 10 keV during quiet and moderate geomagnetic activity. These observations are mostly consistent with the modeled drift paths in Figure 1 [see also *Korth et al.*, 1999], which show this transition occurring between 1 and 10 keV. These observations are also consistent with regions of long (>100 h) drift times shifting from postnoon for 1 keV ions to prenoon for 10 keV ions as shown in *Ferradas et al.* [2016b, Figure 8]. Some discrepancy between observations and model results is reasonable because of the limiting assumptions in our analysis, including a time-stationary electric field model, a strictly dipolar magnetic field model, and our restricting analysis to the equatorial magnetic plane ($K = 0$ in the UBK formalism) despite the small but nonzero inclination of the Van Allen Probes' orbit.

The MLT distributions of 10 keV H^+, He^+, and O^+ are markedly different from the lower energy populations. Fluxes at 10 keV are consistent with dynamics dominated primarily by the gradient-curvature drifts; this manifests in the drastic change in shape of the open trajectory boundary. Ions are transported into the

inner magnetosphere near midnight and postmidnight by a combination of sunward convection and substorm injections and subsequently drift westward/duskward. The eastern edge of the enhancement region is defined by the open trajectory boundary, which is driven to lower L shell with increasing geomagnetic activity and thus allows deep access of ions in the postmidnight region.

4.2. Losses

An observation common across all species, energies, and geomagnetic activity levels is that nightside fluxes tend to be larger than or comparable to dayside fluxes (Figures 3–6). This observation is consistent with particle injection from the plasma sheet on the nightside, and particles undergoing losses as they drift to the dayside. Loss mechanisms include pitch angle scattering, loss to the magnetopause, and for the ion populations, loss due to charge exchange. For the electrons of all energies and 0.1–1 keV ions, the eastern edge of the region of high flux generally lies near late morning or afternoon. A depletion of flux near late afternoon extends toward dusk for these particle populations (identified in the flux distributions as a gap at 1500 MLT). This depletion region is consistent with the open drift paths shown in Figures 1a–1d. Electrons and 0.1–1 keV ions injected on the nightside travel eastward, toward dawn. These particle populations undergo losses along their trajectories; once they approach the noon/dusk sector and continue on toward the magnetopause, significant losses have occurred which correspond to the observed depletion region.

A similar argument describes the formation of the depletion region observed near 10 MLT in the 10 keV ion distributions. The 10 keV ion observations are consistent with the drift paths shown in Figures 1g and 1h. Ions of these energies are injected on the nightside and their drifts are dominated by the effects of the magnetic field. These ions travel westward, toward dusk, along open drift paths. These ions experience losses along their trajectory, and once they reach the morning sector, these losses manifest in the observations as a depletion.

4.3. Ion Abundance Ratio Variability

The relative abundances of H^+, He^+, and O^+ fluxes (Figures 7–9) comprise a systematic study of heavy ion dominance spanning all MLT within geosynchronous orbit; previous similar studies have been limited in scope. We primarily discuss these features in the framework of previous modeling studies which have examined loss rates and drift paths of H^+, He^+, and O^+ in the inner magnetosphere.

At 0.1 and 1 keV, O^+ is dominant during quiet and moderate activity spanning 1800–0900 MLT from L = 2–4 (Figures 7 and 9, left and middle columns). In this same region, a study using Cluster perigee crossings of the magnetic equatorial plane observed no statistically significant O^+ dominance [*Ferradas et al.*, 2015]. However, drift path modeling from that same study indicated He^+ dominance within this region, matching the HOPE observations in this study [see also *Denton et al.*, 2016]. The observed dominance of 0.1 and 1 keV O^+ is consistent with modeling H^+, He^+, and O^+ distributions accounting for losses due to charge exchange, Coulomb energy degradation, and Coulomb scattering [*Jordanova et al.*, 1996]. That same modeling study finds that 1 keV He^+ has longer charge exchange and Coulomb lifetimes than H^+ near midnight. This model and the HOPE data are consistent—1 keV He^+ is observed with equal abundance to H^+ during quiet and moderate geomagnetic activity (Figure 8, middle column).

The abundance of O^+ flux relative to H^+ flux as a function of geomagnetic activity is dependent on L, MLT, and energy; Figure 10 gives the first comprehensive picture of these relationships. Both the H^+ and O^+ flux generally increase with increasing geomagnetic activity (Figures 4 and 5). At L < 5, the increase in H^+ flux generally dominates the increase in O^+ flux and thus the O^+/H^+ flux ratio generally decreases with increasing Kp (Figure 10). This observation is consistent with and expands upon the ISEE-1 study [*Lennartsson and Sharp*, 1982] which showed decreased O^+/H^+ density during disturbed conditions (albeit averaged over all MLT). This observation is inconsistent with *Gloeckler and Hamilton* [1987], although their study was conducted at a much higher energy range (~20–315 keV) than this HOPE study. The dynamics at low L shell are complicated by the motion of the Alfvén boundary, which moves Earthward with increasing activity. During quiet times, particles at low L shell are on closed trajectories and composition is dominated by charge exchange losses. During active times, the Alfvén boundary moves Earthward; regions which were previously closed now have open trajectories and the O^+/H^+ ratio reflects the composition of plasma convected in from the plasma sheet. At higher Kp, convection is stronger and plasma convected from the plasma sheet moves through the system faster than during quiet times. This results in less time for charge exchange to

preferentially deplete H^+ relative to O^+. Modeling of H^+, He^+, and O^+ losses during the beginning of storm recovery corroborate this theory [*Jordanova et al.*, 1996].

At L = 6, the O^+/H^+ ratio generally increases with increasing geomagnetic activity at all energies, which is consistent with numerous previous studies conducted near or beyond geosynchronous orbit [*Lennartsson and Sharp*, 1982; *Young et al.*, 1982; *Lennartsson and Shelley*, 1986; *Gloeckler and Hamilton*, 1987; *Lennartsson*, 1989; *Maggiolo and Kistler*, 2014; *Kistler and Mouikis*, 2016]. A possible exception to this general behavior: although statistics are poor, at 10 keV the O^+/H^+ ratio at 0300–0900 MLT generally decreases with increasing *Kp*.

4.4. The Afternoon Bulge

Mapping the L-MLT structure of the 10 keV O^+ and He^+ afternoon bulge was enabled by the unique measurement capability of the Van Allen Probes HOPE mass spectrometers and the comprehensive L-MLT coverage of the spacecraft orbit. These observations represent the first quantitative study of the afternoon bulge, though previous studies of heavy ion nose structures have hinted at its presence [*Ferradas et al.*, 2015, 2016b]. Cluster perigee crossings of the equatorial plane indicated that heavy ion dominant events are focused in the afternoon and dusk sectors [*Ferradas et al.*, 2015]. However, the highly elliptical nature of the Cluster orbit did not allow for significant counting statistics with full MLT coverage in the equatorial plane, and thus, the boundaries of the afternoon bulge were not visible in that study. The HOPE study of heavy ion nose structures presented by *Ferradas et al.* [2016b] shows that He^+ and O^+ can reach L = ~2–3 in the afternoon sector for low *Kp*. Our comprehensive statistical study of all HOPE particle flux measurements allows for clear identification of the L-MLT structure of the afternoon bulge as seen in Figures 7–9. We observe O^+/H^+ and He^+/H^+ dominance spanning from L = 2–3.75 with the O^+ bulge extending from prenoon to 1930 MLT, beyond the conclusions of the nose structure studies [*Ferradas et al.*, 2015, 2016b]. We observe the afternoon bulge over many orbits during both precessional passes indicating that it is a robust and persistent feature.

Access to the afternoon bulge region by 10 keV plasma sheet ions can be assessed using the access maps in Figures 1i and 1j, and the open trajectory boundaries overlaid on the flux distributions. The afternoon bulge is composed of ions with 10 keV total energy. Comparison of the afternoon bulge in Figures 7–9 with the quiet time 10 keV access map in Figure 1i shows that the bulge lies in the region of 10 keV banana orbits and extends down to regions of closed orbits. Comparison of the in situ measurements with the UBK-derived access maps and open trajectory boundaries assumes that the measured particle distributions are dominated by 90° pitch angle, a reasonable assumption in the inner magnetosphere.

The ion abundance ratios in the afternoon bulge can be explained by drift path modeling and losses due to charge exchange. At ~10 keV the H^+ charge exchange cross section is largest and thus proton losses are maximum [*Jordanova et al.*, 1996]. Thus, it is reasonable to expect an enhancement of both He^+/H^+ and O^+/H^+ as is observed in the afternoon bulge. Furthermore, because the charge exchange cross section of O^+ is larger than for He^+ [*Jordanova et al.*, 1996], we also expect enrichment of He^+ relative to O^+, which is consistent with our observations. However, this line of reasoning does not explain the MLT structure, narrow energy range (observed at 10 keV but not at 3 keV or 30 keV), or the *Kp* dependence of the bulge.

Ferradas et al. [2015, 2016a, 2016b] have developed a drift path model that partially explains these features. Focusing primarily on the HOPE study [*Ferradas et al.*, 2016b], the model calculates bounce-averaged drift trajectories of 90° pitch angle ions at L = 4 using the Volland-Stern electric field model and a dipole magnetic field for *Kp* = 4. Their assumptions are similar to ours, but the restriction to *Kp* = 4 does not allow comparison with observations as a function of geomagnetic activity. Their model shows that plasma sheet ions of energy 17.8 keV have access to L = 2 in the noon, evening, and midnight sectors, whereas 3 and 30 keV ions only penetrate as low as L = 3.5 in these sectors. This narrow energy access is consistent with our observations of the narrow energy range of the afternoon bulge. Their study indicates that access to 1100–2300 MLT occurs for the broadest range in ion energy, meaning that a larger population of ions has access to this region of MLT than to other MLT regions. Neither the modeling of *Ferradas et al.* [2015, 2016b] nor our UBK-derived results fully explain the MLT structure of the afternoon bulge. The UBK formalism used in this study is symmetric across the dawn-dusk meridian. The UBK ion access maps of this study and the drift time and flux loss maps of *Ferradas et al.* [2016b] indicate that He^+ and O^+ should dominate in both the late afternoon sector and in the premidnight sector, with shorter drift times required to access the premidnight sector.

However, Figures 7–9 clearly show that the bulge favors the afternoon sector. Furthermore, neither the UBK formalism nor the drift path modeling accounts for nondipolar deviations of the magnetic field associated with strong geomagnetic activity.

We postulate that the formation of the afternoon bulge may be a product of changing Kp. The afternoon bulge is only observed for $Kp < 5$; however, the 10 keV ion access maps (Figures 1i and 1j) and the open trajectory boundaries in Figures 4 and 5 show that plasma sheet ions on open drift paths have access to L = 2.5 in the dusk sector for $Kp \geq 5$. This is consistent with the drift path modeling of *Ferradas et al.* [2016b], although their modeling study is limited to (a) L-MLT drift time and flux loss maps for $Kp = 4$, and (b) energy-MLT access maps for a range of Kp but limited to L = 4. The limiting assumptions in this drift path modeling study and our own UBK access map study, in particular the time-averaged electric field model, present a simplistic model of very complicated processes in the magnetosphere, and therefore, it is reasonable that plasma sheet particles may have access to L = 2 during geomagnetically active times. During strong convection, the open trajectory access boundary and the Alfvén boundary are pushed Earthward and 10 keV ions have access to the afternoon bulge region. Significant amounts of H^+, He^+, and O^+ would be present during this active time. When convection decreases, particles in this region are trapped on near stagnant (banana) or fully closed drift paths. Differential charge exchange processes can then occur over an extended period, leaving significant He^+, a moderate amount of O^+, and a dearth of H^+.

The combination of UBK-derived ion access maps and drift path modeling [e.g., *Ferradas et al.*, 2016b] explains how these particles might access low L shells and be trapped in the afternoon bulge region but does not account for the well-defined MLT structure of the afternoon bulge. More targeted studies are needed to fully explain these new observations, and specifically, a future study examining the structure of the afternoon bulge as a function of Kp time history is planned.

5. Summary

Using measurements acquired from the two Van Allen Probes precessional orbits spanning October 2012 to February 2016, we have compiled a publicly available, validated survey data set of near-equatorial, omnidirectional fluxes of electrons, H^+, He^+, and O^+ at six energies from 0.1 to 30 keV and for $2 \leq L \leq 6$ as a function of L shell, MLT, and geomagnetic index Kp. Representative flux maps at 0.1, 1, and 10 keV show the structure of different plasma populations, their boundaries, and their variation with geomagnetic activity. These maps are analyzed using a new tool built upon UBK modeling; this tool classifies plasma sheet particle access to the inner magnetosphere for a single energy channel, allowing for useful comparison with in situ data. The primary results of this study are as follows:

1. Inner magnetosphere L-MLT maps of the change in the O^+/H^+ flux ratio with Kp are presented for the first time.
2. The O^+/H^+ ratio at L < 5 generally decreases with Kp at all observed energies; in contrast, the O^+/H^+ ratio at L = 6 generally increases with Kp at all observed energies, consistent with previous studies.
3. A newly identified "afternoon bulge" plasma population enriched in both 10 keV O^+ and He^+ is persistently present for $Kp < 5$ in the MLT sector ~1100–2000 and L shell range 2–4.
4. UBK analysis maps and drift path modeling results are consistent with the narrow energy band and approximate L-MLT location of the afternoon bulge, but the underlying physics describing the detailed structure of the bulge are currently not understood.

Observed spatial distribution and relative composition of hot plasma within the inner magnetosphere (L ~ 2–6) appears largely consistent with a dominant source being the tail plasma sheet, with access to various regions determined by a combination of convective and gradient-curvature drift, and with species-dependent charge exchange lifetimes. We have not addressed the role of specific enhanced-access episodes such as substorm injections [e.g., *Denton et al.*, 2016], but they would be at least reflected statistically in the distributions at higher Kp. Additional results of this study include the following:

1. With increasing geomagnetic activity, high fluxes of 0.1–10 keV ions and electrons penetrate to lower L shell as the Alfvén boundary moves Earthward.
2. At a given geomagnetic activity level, high fluxes of low-energy particles penetrate to lower L shell than higher energy particles.

3. MLT distributions of electron flux at all energies are similar due to the magnetic and electric field drifts acting in the same direction.

4. MLT distributions of ion fluxes are consistent with electric field drifts at energies ≤3 keV and with magnetic field drifts at energies ≥10 keV.

5. Ion and electron fluxes are generally largest at low energies and during geomagnetically active times.

References

Balsiger, H. (1981), Composition of hot ions (0.1–16 keV/e) as observed by the GEOS and ISEE mass spectrometers and inferences for the origin and circulation of magnetospheric plasmas, *Adv. Space Res.*, *I*, 289–303, doi:10.1016/0273-1177(81)90124-1.

Denton, M. H., M. F. Thomsen, H. Korth, S. Lynch, J. C. Zhang, and M. W. Liemohn (2005), Bulk plasma properties at geosynchronous orbit, *J. Geophys. Res.*, *110*, A07223, doi:10.1029/2004JA010861.

Denton, M. H., G. E. Reeves, M. F. Thomsen, M. G. Henderson, R. H. W. Friedel, B. Larsen, R. M. Skoug, H. O. Funsten, H. E. Spence, and C. A. Kletzing (2016), The complex nature of storm-time ion dynamics: Transport and local acceleration, *Geophys. Res. Lett.*, *43*, 1–9, doi:10.1002/2016GL070878.

Ejiri, M. (1978), Trajectory traces of charged particles in the magnetosphere, *J. Geophys. Res.*, *83*(A10), 4798–4810, doi:10.1029/JA083iA10p04798.

Ejiri, M., R. A. Hoffman, and P. H. Smith (1980), Energetic particle penetrations into the inner magnetosphere, *J. Geophys. Res.*, *85*(A2), 653–663, doi:10.1029/JA085iA02p00653.

Ferradas, C. P., J. C. Zhang, L. M. Kistler, and H. E. Spence (2015), Heavy-ion dominance near cluster perigees, *J. Geophys. Res. Space Physics*, *120*, 10,485–10,505, doi:10.1002/2015JA021063.

Ferradas, C. P., J.-C. Zhang, H. E. Spence, L. M. Kistler, B. A. Larsen, G. Reeves, R. Skoug, and H. Funsten (2016a), Drift paths of ions composing multiple-nose spectral structures near the inner edge of the plasma sheet, *Geophys. Res. Lett.*, *43*, 11,411–11,492, doi:10.1002/2016GL071359.

Ferradas, C. P., J.-C. Zhang, H. E. Spence, L. M. Kistler, B. A. Larsen, G. Reeves, R. Skoug, and H. Funsten (2016b), Ion nose spectral structures observed by the Van Allen Probes, *J. Geophys. Res. Space Physics*, *121*, 12,025–12,046, doi:10.1002/2016JA022942.

Fok, M.-C., R. A. Wolf, R. W. Spiro, and T. E. Moore (2001), Comprehensive computational model of Earth's ring current, *J. Geophys. Res.*, *106*(A5), 8417–8424, doi:10.1029/2000JA000235.

Forster, D. R., M. H. Denton, M. Grande, and C. H. Perry (2013), Inner magnetospheric heavy ion composition during high-speed stream-driven storms, *J. Geophys. Res. Space Physics*, *118*, 4066–4079, doi:10.1002/jgra.50292.

Friedel, R. H. W., H. Korth, M. G. Henderson, M. F. Thomsen, and J. D. Scudder (2001), Plasma sheet access to the inner magnetosphere, *J. Geophys. Res.*, *106*(A4), 5845–5858, doi:10.1029/2000JA003011.

Friedel, R. H. W., G. D. Reeves, and T. Obara (2002), Relativistic electron dynamics in the inner magnetosphere—A review, *J. Atmos. Sol. Terr. Phys.*, *64*(2), 265–282, doi:10.1016/S1364-6826(01)00088-8.

Fu, S. Y., Q.-G. Zong, B. Wilken, and Z. Y. Pu (2001), Temporal and spatial variation of the ion composition in the ring current, *Space Sci. Rev.*, *95*(1970), 539–554, doi:10.1023/A:1005212906199.

Funsten, H. O., R. W. Harper, and D. J. McComas (2005), Absolute detection efficiency of space-based ion mass spectrometers and neutral atom imagers, *Rev. Sci. Instrum.*, *76*(5), 053301, doi:10.1063/1.1889465.

Funsten, H. O., et al. (2013), Helium, Oxygen, Proton, and Electron (HOPE) mass spectrometer for the radiation belt storm probes mission, *Space Sci. Rev.*, *179*(1), 423–484, doi:10.1007/s11214-013-9968-7.

Fuselier, S. A., R. C. Elphic, and J. T. Gosling (1999), Composition measurements in the dusk flank magnetosphere, *J. Geophys. Res.*, *104*(A3), 4515–4522, doi:10.1029/1998JA900137.

Geiss, J., H. Balsiger, P. Eberhardt, H. P. Walker, L. Weber, D. T. Young, and H. Rosenbauer (1979), Dynamics of magnetospheric ion composition as observed by the GEOS mass spectrometer, in *Advances in Magnetosperic Physics with GEOS-1 and ISEE*, edited by K. Knott, A. Durney, and K. Ogilvie, pp. 217–246, Springer, Dordrecht, Netherlands.

Gendrin, R. (1975), Waves and wave-particle interactions in the magnetosphere: A review, *Space Sci. Rev.*, *18*, 145–200, doi:10.1007/BF00172533.

Gloeckler, G., and D. C. Hamilton (1987), AMPTE ion composition results, *Phys. Scr.*, *T18*, 73–84, doi:10.1088/0031-8949/1987/T18/009.

Gomberoff, L., and R. Neira (1983), Convective growth rate of ion cyclotron waves in a H^+-He^+ and H^+-He^+-O^+ plasma, *J. Geophys. Res.*, *88*(2), 2170–2174, doi:10.1029/JA088iA03p02170.

Johnson, R. G. (1979), Energetic ion composition in the Earth's magnetosphere, *Rev. Geophys. Space Phys.*, *17*(4), 4495–4502, doi:10.1029/RG017i004p00696.

Johnson, R. G., R. D. Sharp, and E. G. Shelley (1975), Composition of the hot plasmas in the magnetosphere, in *Physics of the Hot Plasma in the Magnetosphere*, edited by B. Hultqvist and L. Stenflo, pp. 45–68, Springer, Boston, Mass.

Jordanova, V. K., L. M. Kistler, J. U. Kozyra, G. V. Khazanov, and A. F. Nagy (1996), Collisional losses of ring current ions, *J. Geophys. Res.*, *101*(A1), 111–126, doi:10.1029/95JA02000.

Kistler, L. M., and C. G. Mouikis (2016), The inner magnetosphere ion composition and local time distribution over a solar cycle, *J. Geophys. Res. Space Physics*, *121*, 2009–2032, doi:10.1002/2015JA021883.

Kistler, L. M., et al. (2016), The source of O+ in the storm time ring current, *J. Geophys. Res. Space Physics*, *121*, 5333–5349, doi:10.1002/2015JA022204.

Korth, H., M. F. Thomsen, J. E. Borovsky, and D. J. McComas (1999), Plasma sheet access to geosynchronous orbit, *J. Geophys. Res.*, *104*(A11), 25,047–25,061, doi:10.1029/1999JA900292.

Kozyra, J. U., T. E. Cravens, A. F. Nagy, E. G. Fontheim, and R. S. B. Ong (1984), Effects of energetic heavy ions on electromagnetic ion cyclotron wave generation in the plasmapause region, *J. Geophys. Res.*, *89*(A4), 2217, doi:10.1029/JA089iA04p02217.

Lennartsson, W. (1989), Energetic (0.1- to 16-keV/e) magnetospheric ion composition at different levels of solar F10.7, *J. Geophys. Res.*, *94*(A4), 3600–3610, doi:10.1029/JA094iA04p03600.

Lennartsson, W., and R. D. Sharp (1982), A comparison of the 0.1-17 keV/e ion composition in the near equatorial magnetosphere between quiet and disturbed conditions, *J. Geophys. Res.*, *87*, 6109–6120, doi:10.1029/JA087iA08p06109.

Lennartsson, W., and E. G. Shelley (1986), Survey of 0.1- to 16-keV/e plasma sheet ion composition, *J. Geophys. Res.*, *91*(A3), 3061–3076, doi:10.1029/JA091iA03p03061.

Lennartsson, W., E. G. Shelley, R. D. Sharp, R. G. Johnson, and H. Balsiger (1979), Some initial ISEE-1 results on the ring current composition and dynamics during the magnetic storm of December 11, 1977, *Geophys. Res. Lett.*, *6*(6), 483–486, doi:10.1029/GL006i006p00483.

Lennartsson, W., R. D. Sharp, E. G. Shelley, R. G. Johnson, and H. Balsiger (1981), Ion composition and energy distribution during 10 magnetic storms, *J. Geophys. Res.*, *86*(A6), 4628–4638, doi:10.1029/JA086iA06p04628.

Leske, R. A., and M. E. Wiedenbeck (1993), Composition measurements from ISEE-3: Fluorine through calcium, in *23rd International Cosmic Ray Conference at University of Calgary*, *Alberta*, p. 571.

Liu, W. L., S. Y. Fu, Q. Zong, Z. Y. Pu, J. Yang, and P. Ruan (2005), Variations of N+ / O+ in the ring current during magnetic storms, *Geophys. Res. Lett.*, *32*, L1510, doi:10.1029/2005GL023038.

Maggiolo, R., and L. M. Kistler (2014), Spatial variation in the plasma sheet composition: Dependence on geomagnetic and solar activity, *J. Geophys. Res. Space Physics*, *119*, 2836–2857, doi:10.1002/2013JA019517.

Mannucci, A. J., B. T. Tsurutani, M. C. Kelley, B. A. Iijima, and A. Komjathy (2009), Local time dependence of the prompt ionospheric response for the 7, 9, and 10 November 2004 superstorms, *J. Geophys. Res.*, *114*, A11315, doi:10.1029/2009JA014043.

Mauk, B. H., N. J. Fox, S. G. Kanekal, R. L. Kessel, D. G. Sibeck, and A. Ukhorskiy (2013), Science objectives and rationale for the Radiation Belt storm probes mission, *Space Sci. Rev.*, *179*, 3–27, doi:10.1007/s11214-012-9908-y.

Maynard, N. C., and A. J. Chen (1975), Isolated cold plasma regions: Observations and their relation to possible production mechanisms, *J. Geophys. Res.*, *80*(7), 1009–1013, doi:10.1029/JA080i007p01009.

McIlwain, C. E. (1963), The radiation belts, natural and artificial, *Science*, *142*(3590), 355–361, doi:10.1126/science.142.3590.355.

Morley, S. K., M. G. Henderson, G. D. Reeves, R. H. W. Friedel, and D. N. Baker (2013), Phase space density matching of relativistic electrons using the Van Allen Probes: REPT results, *Geophys. Res. Lett.*, *40*, 4798–4802, doi:10.1002/grl.50909.

Nishimura, Y., A. Shinbori, T. Ono, M. Iizima, and A. Kumamoto (2007), Evolution of ring current and radiation belt particles under the influence of storm-time electric fields, *J. Geophys. Res.*, *112*, A06241, doi:10.1029/2006JA012177.

Olson, P. W., and K. Pfitzer (1977), *Magnetospheric Magnetic Field Modeling*, AFOSR-TR-77-0156, McDonnell Douglas Astronaut Co., Huntington Beach, Calif.

Perry, C. H., M. Grande, A. M. Hall, and B. Wilken (1996), Statistical survey of dispersionless substorm injections observed by the CRRES MICS ion spectrometer, in *International Conference on Substorms*, *Proceedings of the 3rd International Conference held in Versailles*, p. 567.

Pfitzer, K. A., and J. R. Winckler (1968), Experimental observation of a large addition to the electron inner radiation belt after a solar flare event, *J. Geophys. Res.*, *73*(17), 5792–5797, doi:10.1029/JA073i017p05792.

Ridley, A. J., and M. W. Liemohn (2002), A model-derived storm time asymmetric ring current driven electric field description, *J. Geophys. Res.*, *107*(A8), SMP 2-1–SMP 2-12, doi:10.1029/2001JA000051.

Roederer, J. G., and H. Zhang (2014) *Dynamics of Magnetically Trapped Particles*, 2nd ed., Springer, Berlin.

Rowland, D. E., and J. R. Wygant (1998), Dependence of the large-scale, inner magnetospheric electric field on geomagnetic activity, *J. Geophys. Res.*, *103*(A7), 14,959–14,964, doi:10.1029/97JA03524.

Sarno-Smith, L. K., B. A. Larsen, R. M. Skoug, M. W. Liemohn, A. Breneman, J. R. Wygant, and M. F. Thomsen (2016), Spacecraft surface charging within geosynchronous orbit observed by the Van Allen Probes, *Space Weather*, *14*, 151–164, doi:10.1002/2015SW001345.

Sheldon, R. B., and H. E. Spence (1997), Alfvén boundaries: Noses and zippers, *Adv. Space Res.*, *20*(3), 445–448, doi:10.1016/S0273-1177(97)00708-4.

Singh, A. K., R. P. Singh, and D. Siingh (2011), State studies of Earth's plasmasphere: A review, *Planet. Space Sci.*, *59*(9), 810–834, doi:10.1016/j.pss.2011.03.013.

Smith, P. H., and R. A. Hoffman (1974), Direct observations in the dusk hours of the characteristics of the storm time ring current particles during the beginning of magnetic storms, *J. Geophys. Res.*, *79*(7), 966–971, doi:10.1029/JA079i007p00966.

Sojka, J. J., R. W. Schunk, J. F. E. Johnson, J. H. Waite, and C. R. Chappell (1983), Characteristics of thermal and suprathermal ions associated with the dayside plasma trough as measured by the dynamics explorer retarding ion mass spectrometer, *J. Geophys. Res.*, *88*(3), 7895–7911.

Spence, H. E., et al. (2013), Science goals and overview of the radiation belt storm probes (RBSP) energetic particle, composition, and thermal plasma (ECT) suite on NASA's Van Allen Probes mission, *Space Sci. Rev.*, *179*(1), 311–336, doi:10.1007/s11214-013-0007-5.

Stern, D. P. (1975), The motion of a proton in the equatorial magnetosphere, *J. Geophys. Res.*, *80*(4), 595–599, doi:10.1029/JA080i004p00595.

Strangeway, R. J., and R. G. Johnson (1984), Energetic ion mass composition as observed at near-geosynchronous and low altitudes during the storm period of February 21 and 22, 1979, *J. Geophys. Res.*, *89*(A10), 8919–8939, doi:10.1029/JA089iA10p08919.

Thomsen, M. F. (2004), Why *Kp* is such a good measure of magnetospheric convection, *Space Weather*, *2*, S11004, doi:10.1029/2004SW000089.

Thorne, R. M. (2010), Radiation belt dynamics: The importance of wave-particle interactions, *Geophys. Res. Lett.*, *37*, L22107, doi:10.1029/2010GL044990.

Volland, H. (1973), A semiempirical model of large-scale magnetospheric electric fields, *J. Geophys. Res.*, *78*(1), 171–180, doi:10.1029/JA078i001p00171.

Whipple, E. C. (1978), (U, B, K) Coordinates: A natural system for studying magnetospheric convection, *J. Geophys. Res.*, *83*(A9), 4318–4326, doi:10.1029/JA083iA09p04318.

Whipple, E. C., et al. (1998), Identification of magnetospheric particles that travel between spacecraft and their use to help obtain magnetospheric potential distributions, *J. Geophys. Res.*, *103*(A1), 93–102, doi:10.1029/97JA02195.

Wilken, B., W. Weiss, D. Hall, M. Grande, F. Soraas, and J. F. Fennell (1992), Magnetospheric ion composition spectrometer onboard the CRRES spacecraft, *J. Spacecr. Rocket.*, *29*(4), 585–591, doi:10.2514/3.25503.

Williams, D. J. (1981), Ring current composition and sources: An update, *Planet. Space Sci.*, *29*(11), 1195–1203, doi:10.1016/0032-0633(81)90124-0.

Young, D. T. (1983), Near-equatorial magnetospheric particles from ~1 eV to ~1 MeV, *Rev. Geophys.*, *21*(2), 402–418, doi:10.1029/RG021i002p00402.

Young, D. T., S. Perraut, A. Roux, C. D. Villedary, R. Gendrin, A. Korth, G. Kremser, and D. Jones (1981), Wave-particle interactions near $\Omega_{\text{He+}}$ observed on GEOS 1 and 2. Propagation of ion cyclotron waves in He$^+$-rich plasma, *J. Geophys. Res.*, *86*(A8), 6755–6772, doi:10.1029/JA086iA08p06755.

Young, D. T., H. Balsiger, and J. Geiss (1982), Correlations of magnetospheric ion composition with geomagnetic and solar activity, *J. Geophys. Res.*, *87*(A11), 9077, doi:10.1029/JA087iA11p09077.